MASTER

Design through Analysis of 3D Printed Fluid Devices

Peng, F.

Award date:
2018

TU/e Technische Universiteit
Eindhoven
University of Technology

Department of Mechanical Engineering
Energy Technology and Fluid Dynamics Group

Design through Analysis of
3D Printed Fluid Devices

Fankai Peng
ID: 1038461
Master: Mechanical Engineering
Research Group: Energy Technology

Supervisor:
dr.ir. C.V. Verhoosel

Eindhoven, July 2018

Contents

Chapter 1

Introduction

Additive manufacturing, a production process also known as 3D printing, has been in the spotlight in recent years as an advanced technology in the manufacturing industry. Applications of the technology explode with the fast growth of the market due to advantages including high production rates and improving production qualities. Employment of numerical analysis in additive manufacturing can promote the productivity even further. One special situation is in the manufacturing of fluid devices, where channels instead of solids themselves are significant. In this project, numerical simulations on 3D printed fluid devices are investigated. Currently, an integrated workflow for the design, analysis, and testing of such devices is not generally available. This research project contributes to the development of such a workflow by integrating the design and numerical analysis steps. Research has been conducted on models of the Tesla valve, a type of fixed-geometry passive check valve without moving parts, which allows flow in only one direction.

This introductory chapter is outlined as follows. The principle of the Tesla valve will be introduced briefly in Section 1.1. Section 1.2 presents a concise introduction to the Finite Cell Method, the simulation technology which is at the heart of the numerical analyses considered in this thesis. A preliminary experiment is presented in Section 1.3 and corresponding preliminary numerical simulations are demonstrated in Section 1.3.2. This introduction is concluded with a discussion of the objectives and outline of this thesis.

1.1   The Tesla valve

An example of the Tesla valve is shown in Fig. 1.1. The Tesla valve was firstly introduced by N. Tesla [35] as a "valvular conduit". Tesla valves can be used for either forward or reverse flow. The forward flow in a Tesla valve is more resisted than the reverse flow. The working principle of the Tesla valve is based on the distribution of the flow [3]. The flow through the side channel requires significant work to redirect the downstream or to combine with the flow in the main channel. Distribution also leads to high shear regions at junctions. For laminar flows, this behavior is the main source of the direction dependent resistance. The inertia of the flow is important and the resistance behavior is inherently influenced by the Reynolds number. Forster [6] in 1995 experimentally compared Tesla type valves with various diffuser type valves. All these valves are without any moving parts and the channels are with direction dependent flow resistance. A typical model of the Tesla valve was proposed in [6]. The model is referred to as the T45-R because the internal angle α (see Fig. 1.2) is set to 45 degrees.

The property that a Tesla valve promotes flow in one direction over the other one can be evaluated by the property diodicity called Di. Di is defined as the ratio of the pressure difference across the
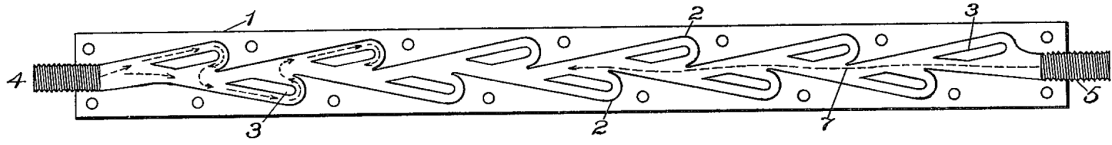
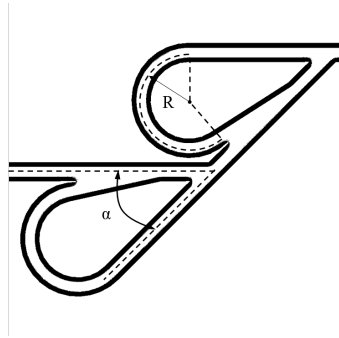Figure 1.1: Cross Section of a Tesla Valve. Image from Ref. [35]

Figure 1.2: Definition of some shape related parameters for T45-R Tesla valves

valve in the reverse direction over that in the forward direction at a specific flow rate,

$$Di = \frac{\Delta p_r}{\Delta p_f} \tag{1.1}$$

where the subscripts r and f refer to the reverse and forward directions, respectively.

Numerous researche efforts have investigated the optimization of Tesla valves. For the T45-R Tesla valve, the diodicity is found to increase linearly with the flow rate for low Reynolds numbers (below approximately 300) [6]. Truong et al. [37] proposed an inversely proportional relation between the diodicity and the radius R (defined as in Fig. 1.2), and quantified how the diodicity is related to the optimal angle α and the characteristic length, which is generally the width of channels in Tesla valves. According to the presented results the obtained conclusions are valid for Reynolds number ranging from 100 to 600. Zhang et al. [43] concluded that square cross-sectioned channels yielded the maximum diodicity for low Reynolds numbers ($Re < 500$) based on three-dimensional (3D) flow simulations on the T45-R valve, and that a linear relationship exists between the channel aspect ratio and the diodicity.

In addition to the T45-R Tesla valve, Liao et al. [18] proposed a potential option of a Tesla valve labelled MT135 (as shown in Fig. 1.3), for which the internal angle equals to 135 degrees instead of 45. Gamboa [7] accomplished the optimization of the valve shape further by dynamic parameter determination and achieved a significant increase in the calculated diodicity compared to the T45-R valve by a maximum of 37% at $Re = 2000$. An average increase of 25% over the range $0 < Re < 2000$ was also demonstrated. These research efforts proved the feasibility of improving the performance of a single Tesla valve by geometry optimization.

Besides investigations on the optimization of a single Tesla valve, the in-series configuration of multiple, identically shaped Tesla valves has been studied. Multistage Tesla valve (MSTV) manifestes higher flow rates compared to the single stage Tesla valves. Tesla [35] in his patent presented
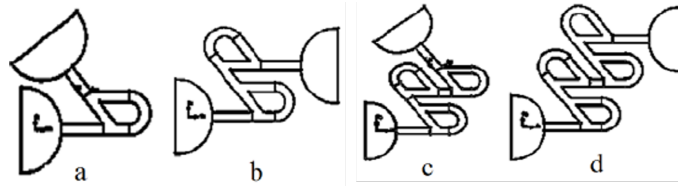
Figure 1.3: Different layout used for MT135 microvalve: (a) one stage (b) two staged (c) three staged (d) four staged. Figure from Ref. [36]

a set of valvular conduits in sequence and claimed that additional stages increase the diodicity. Reed and Fla [28] experimentally proved that for a T45-R Tesla valve, the diodicity doubles when the number of valves was increased from 1 to 2, and additional stages increased the pressure drop but did not change the diodicity enormously. Mohammadzadeh et al. [23] stated that the diodicity of MSTV increased with the number of stages in Tesla valves only when Reynolds numbers were greater than 50. Thompson et al. [36] addressed the influence of the Reynolds number, the number of valves and the distance between valves on the diodicity based on simulations. According to them, the diodicity of the MSTV increases nonlinearly with an increasing Reynolds number. For a relatively large Reynolds number, the diodicity increases with the number of stages, and it decreases with the valve-to-valve distance.
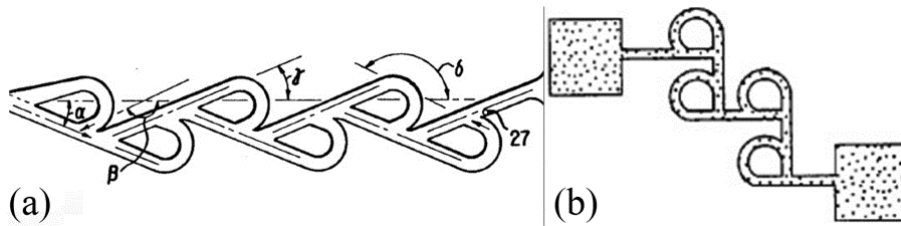
Figure 1.4: Multistage Tesla valve (MSTV) with (a) low-angled configuration. Figure from Ref. [28] and (b) high-angled configuration. Figure from Ref. [1]

This thesis focuses on the numerical analysis of Tesla valves with immmersed isogeometric analysis and on the integration between CAD files and numerical analyses. While parametric design of the Tesla valve is an important topic, the conventional T45-R geometry is utilized in most simulations to validate the proposed analysis methods. The T45-R Tesla valve appeals for lower pressure loss in the forward direction compared with Tesla valves of larger inner angles, thus promoting potential applications. Thompson et al. [36] addressed that for multistage Tesla valves, local transitional and turbulent flow occurred at junctions even when the flow was laminar at the valve inlet ($Re < 2300$). The Reynolds number at the valve inlet was around 300 when the transitional flow occurred. In order to simplify simulation problems and to focus on the main topic of research, parameters in our simulations are controlled such that the Reynolds number is always under 300 at the inlet and convection-dominated effects and turbulence can be ignored.

1.2 Immersed finite elements: The Finite Cell Method

Flow in a Tesla valve follows the geometry of the channel, which in general is quite complex. In contrast to many traditional numerical methods that require conforming meshes, immersed boundary methods avoid complicated mesh generation. This makes such immersed analysis tools attractive to use in complicated geometric configurations such as Tesla valves.

Design through Analysis of 3D Printed Fluid Devices

The concept "immersed boundary method" was first proposed by Peskin [25]. For blood flow problems associated with cardiac mechanics, where flow interacts with the surrounding solid material, conventional numerical analysis techniques employ grids conforming to the boundary. Since the grid generation for complex geometry is costly, Peskin proposed the concept "fictitious domains" and employed non-conforming Cartesian grids on complex geometries. The solid boundaries were then imposed by modification of the governing equations. Distinguished by the implementation of the modifications, immersed methods are divided into continuous forcing approaches and discrete forcing approaches [22].

The Finite Cell method is a typical immersed boundary method and is one of the continuous forcing approaches. With the concept of "fictitious domain", Parvizian and Rank proposed the Finite Cell Method (FCM) [24]. In the FCM, the physical domain Ω_{phy} is extended with a fictitious domain Ω_{fict}, which is generally a simple shape such as a rectangle (as shown in Fig. 1.5). With the help of the extended domain, time-consuming and error-prone conforming mesh generation for complex domains is eliminated and the possibility for a seamless integration of complex geometric models and finite element analysis is therefore promoted. The regular mesh $\mathcal{T}_{\mathcal{A}}^{\langle}$ covering the complete ambient domain can be easily generated and a discretization space for Galerkin's method on the ambient mesh can be constructed.

The accuracy of the FCM can be controlled as optimal rates of convergence are obtained under mesh refinement and exponential convergence with increasing the polynomial degrees. Natural boundary conditions in the FCM can be straightforwardly achieved, but essential boundary conditions require weak imposition. Details can be found in Section 2.4 where weak imposition of periodic boundary conditions is discussed.
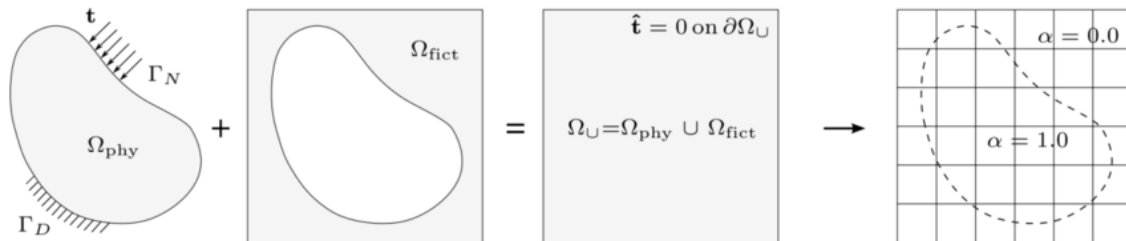
Figure 1.5: The physical domain on the left Ω_{phy} is extended with Ω_{fict} and a regular mesh is generated on the complete ambient domain $\Omega_{\cup}$. The physical domain is distinguished by the variable α which is 1 in it and 0 outside. Figure from Ref. [24]

1.3 Preliminary example

1.3.1 Experiment

To get a basic impression of the Tesla valve, a preliminary experiment is conducted on a 3D printed Tesla Valve. For this experiment a CAD model is built and a experimental setup is designed with a 3D printed Tesla valve (Fig. 1.6).

Air flow generated from the air pump flows through the Tesla valve and goes into the atmosphere. The pressure at the inlet of the Tesla valve is measured by the pressure meter. This value also equals the pressure drop across the Tesla valve ignoring the pressure change due to the flow meter and the connecting tubes. The pressure drops for different flow rates are recorded and compared.

(a)

(b)

(c) port labels

Figure 1.6: Diagram of the experimental setup. The air flow generated by the air pump goes through the Tesla valve, the flow meter and finally goes into the atmosphere.

The diodicity Di defined in Eq. 1.1 is then calculated and analyzed. The cross section of the channel in the model is 5mm $\times$ 5mm square. The maximum flow rate along the channel is:

$$u = \frac{q}{A} \approx \frac{50 \quad l/min}{(5 \times 10^{-3} \quad m)^2} \tag{1.2}$$
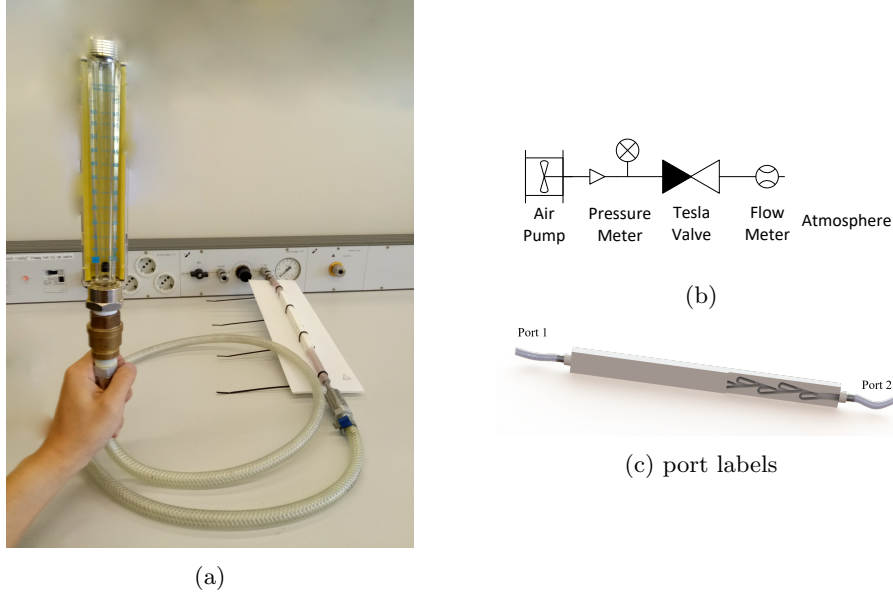
$$= \frac{50 \times 10^{-3}}{2.5^{-5} \quad m^2 \times 60 \quad s} \tag{1.3}$$

$$= 33 \quad m/s \tag{1.4}$$

The Reynolds number in this experiment is:

$$Re = \frac{u \cdot L}{\nu} = \frac{33 \times 5 \times 10^{-3}}{15 \times 10^{-6}} \approx 11000 \tag{1.5}$$

where ν is the kinematic viscosity.

This theoretical maximum Reynolds number in this experiment is quite large. Given the flow rate is generally smaller and that some air is leaking, the actual Reynolds number is anticipated to be lower. However, the basic physical phenomena are assumed to be represented by this experimental setup. The experiment can be further improved if the air-tightness of the devices is taken into consideration.

The relation between the pressure drop and flow rates for flow in different directions is shown in Fig. 1.7, from which we observe that:

1. For a constant pressure drop, the velocity of the flow in the direction $port1 \rightarrow port2$ (see Fig. 1.6c) is always higher than that in the reverse direction.

2. For increasing pressure drop, the flow in the direction $port1 \rightarrow port2$ (see Fig. 1.6c) increases faster than the flow in the reverse direction.

This Tesla valve experiment demonstrates little restriction of the flow in one direction in comparison to the flow in the reverse direction. The flow resisting properties described in the literature
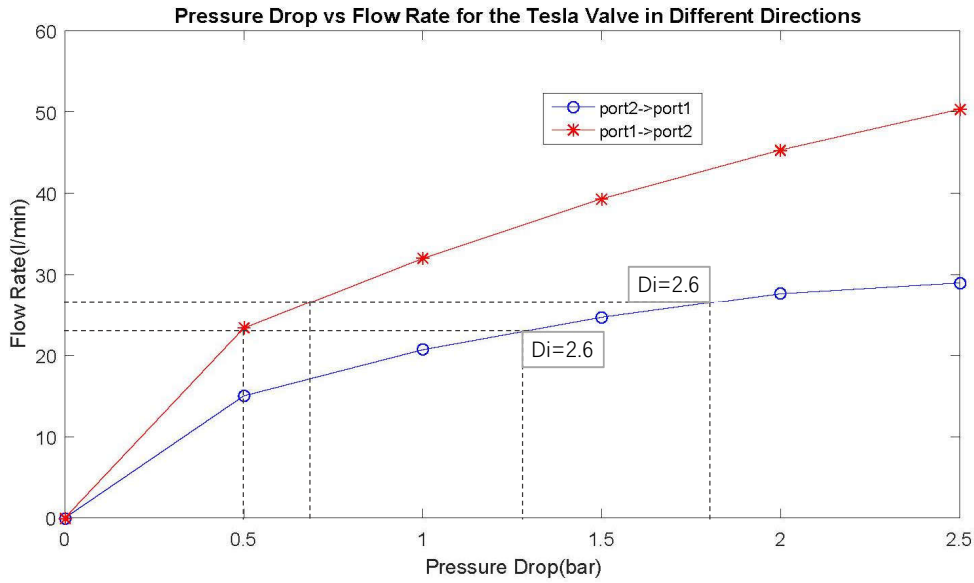
Figure 1.7: Relation of the pressure drops and the flow rates when the Tesla valve is employed in different directions.

are well verified by our observations. Ideally, the diodicity would also be observed in simulations. Preliminary numerical simulations of flow through the Tesla valve are studied in Section 1.3.2.

1.3.2 Mesh-conforming finite element analysis

To illustrate the complications associated with mesh-conforming analyses, and hence to motivate the usage of the Finite Cell Method in this graduation project, we study the steady Navier-Stokes problem for the flow in the Tesla valve in Section 1.3 using a mesh conforming finite element method.

Figure 1.8: Geometry of the simplified computational domain of the Tesla valve.

To simplify the problem, we here consider incompressible flow instead of compressible air flow. The geometry of the Tesla valve is simplified to a planar surface $\Omega \in \mathbb{R}^2$ (see Fig. 1.8). The boundary $\partial\Omega$ consists of Γ_{wall}, Γ_{in} and Γ_{out}. Γ_{wall} is subject to a Dirichlet boundary condition where all velocity components are set to zero. A parabolic horizontal velocity profile f is imposed on the Dirichlet boundary Γ_{in}, which is located on the left or the right boundary, depending on whether the normal flow or the reverse flow is considered. Γ_{out} is a traction free outlet. $\mathbf{n}$ denotes the outward-pointing unit vector normal to $\partial\Omega$. The Navier-Stokes equations for the velocity field

$\mathbf{u} : \Omega \to \mathbb{R}^2$ and pressure field $p : \Omega \to \mathbb{R}$ read:

$$
\begin{cases}
\text{Find} \quad \mathbf{u} : \Omega \to \mathbb{R}^2, \quad p : \Omega \to \mathbb{R} \quad \text{such that,} \\
\rho \nabla \cdot (\mathbf{u} \otimes \mathbf{u}) - \mu \nabla \cdot (\nabla^s \mathbf{u}) + \nabla p = \quad 0 \quad \text{in} \quad \Omega, \\
\nabla \cdot \mathbf{u} = \quad 0 \quad \text{in} \quad \Omega, \\
\mathbf{u} = \quad 0 \quad \text{on} \quad \Gamma_{wall}, \\
\mathbf{u} = \quad \mathbf{f} \quad \text{on} \quad \Gamma_{in}, \\
2\mu \nabla^s \mathbf{u} \cdot \mathbf{n} - p\mathbf{n} = \quad 0 \quad \text{on} \quad \Gamma_{out},
\end{cases}
\tag{1.6}
$$

Here μ represents the dynamic viscosity of the flow. The density and the viscosity are assigned the values of liquid water. The average velocity at the inlet equals 10 mm/s. The characteristic length equals the width of the channel and is 5 mm. The Reynolds number Re equals 25.

For the mesh conforming analysis considered here, the CAD file in the IGS format is imported into the open source meshing tool Gmsh to generate a conforming mesh. Processing of the CAD data file results in divided arcs in Gmsh as shown in Fig. 1.9. The built-in data structures lead to redundant usage of memory. The meshing process, which is assumed to be automatic, requires manual operations including definition of physical entities. The definition of physical entities consists of the selection of the the physical domain and the connection between geometric entities and different boundary conditions. This is not a trivial step, since selection of several geometry entities from in total 400 entities requires great patience, even for a simplified two dimensional geometry as considered in this example.
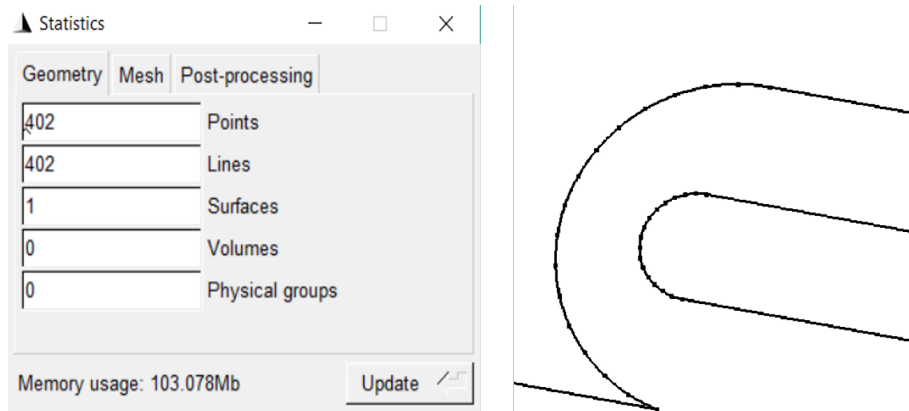
Figure 1.9: Statistic information in Gmsh for the simplified Tesla geometry (left). Divided arcs (right).

Simulation with boundary conditions defined in Fig. 1.10 produces velocity and pressure schemes as shown in the Fig. 1.11. Peaks in the velocity appear at the junctions, and the maximum velocity in the reverse flow is larger than that in the forward flow. While the simulations for flows in two different directions are conducted under the same velocity schemes at the inlet, it is shown in the pressure plots that the pressure drop in the reverse flow is higher than the forward flow, with the diodicity around $Di = \frac{14.5}{8.5} = 1.7$.

The diodicity obtained from the simulation is above 1. This explains that the pressure difference is higher in the reverse flow compared to the forward flow. The results (in Fig. 1.11) are reasonable. However, the procedure with which they are obtained is labour intensive. Every trivial change in the shape or in the mesh requires the generation of a new mesh. Hence, a study of the quality of the numerical result by mesh convergence studies is impractical, as is the study of geometry optimization.

Figure 1.10: Mesh of the simplified computational domain of the Tesla valve.

(a) Velocity profile as the result of the simulation.

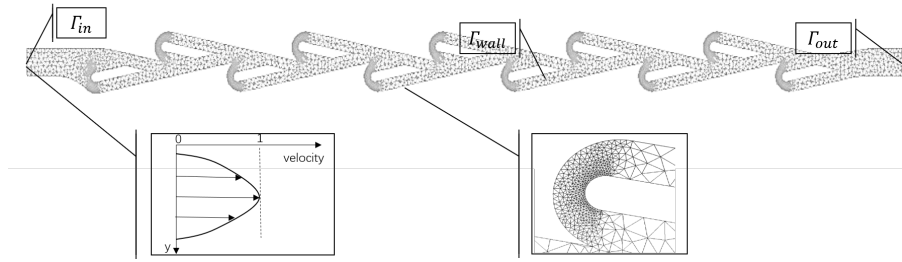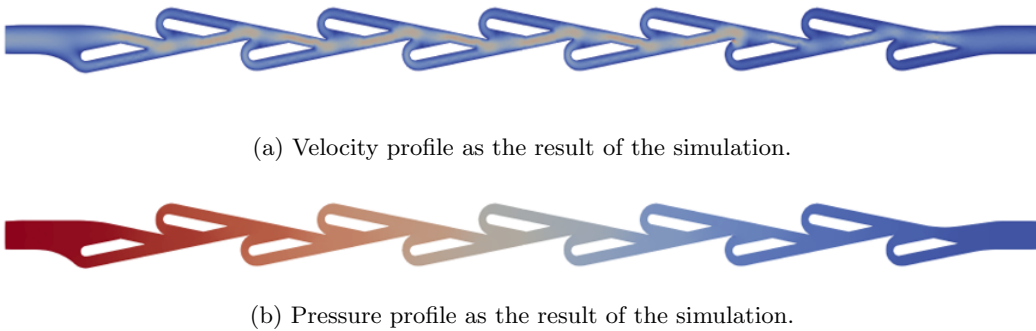(b) Pressure profile as the result of the simulation.

Figure 1.11: Results of simulation analyzed with the conventional method.

1.4 Objective, scope and outline

The main goal of this thesis is to develop a workflow integrating design and numerical analysis steps, based on the immersogeometric analysis framework. The proposed workflow should be applicable to flow problems for two- and three-dimensional Tesla valves. To achieve this overall goal, we identify the following objectives:

1. We aim to specify necessary adjustments in the immersogeometric analysis framework to make it compatible with flow problems for Tesla valves. The imposition of boundary conditions is one aspect on which we focus in particular.

2. We aim to develop an approach to utilize CAD data files directly in numerical analyses. Our goal is to find a way to reconstruct geometry which can be used in the Finite Cell Method from CAD data files and to clarify implementation details.

3. To give a demonstration of the proposed work flow, we plan to conduct analyses of two- and three- dimensional Tesla valves by investigation of models with various shape improvements.

Our scope focuses on incompressible fluid flows, in particular the steady Stokes equations and the steady Navier-Stokes equations. Limited by computing abilities, convection-dominated flow problems are out of our scope and only problems with moderate Reynolds numbers are considered. Since this thesis focuses mainly on application aspects, mathematical analysis of the proposed workflow is not elaborated in detail.

In this report, applications of the immersed method and the isogeometric analysis method for problems of the flow in Tesla valves are investigated. An integrated workflow starting from CAD data files and working with the immersed isogeomertic analysis method is proposed. Chapter 2

discusses applications of the immersogeometric analysis method on flow problems in Tesla valves. Chapter 3 proposes a workflow relating CAD data files to numerical analysis. Chapter 4 provides applications of the workflow in the shape improvement of Tesla valves. Conclusions are finally drawn in Chapter 5.

Chapter 2

Immersogeometric analysis

In this chapter we introduce the formulation and implementation of the immersogeometric analysis framework considered in this thesis. We propose a formulation to weakly impose periodic boundary conditions using Nitsche's method. A test case considering an incompressible steady Navier-Stokes flow problem is considered to demonstrate the technique and a convergence study is conducted to understand the method.

This chapter is outlined as follows. The background of isogeometric analysis is given in section 2.1. The integration of IGA with the immersed Finite Cell method and the required stabilization techniques are described in section 2.2. The formulation of the problem is discussed in section 2.3. The weak imposition of periodic boundary conditions is proposed in section 2.4. Finally, the proposed method is demonstrated using a numerical example in the section 2.5.

2.1 Isogeometric analysis

IsoGeometric analysis (IGA) was introduced by Hughes et al. [14] as a novel framework to establish a straight-forward interaction between computer aided design (CAD) and finite element analysis (FEA). The fundamental idea of IGA is that it uses basis functions obtained from CAD modeling such as B-splines and non-uniform rational B-splines (NURBS). The smoothness property of higher order B-spline basis functions allows to achieve higher-order continuity. IGA has been applied for a wide variety of applications including solid mechanics [21], fluid dynamics [11] and multi-physics modeling [4]. The construction of B-splines, which form the fundamental building block of isogeometric analysis, is discussed in the following paragraph.

B-spline basis The B-spline basis functions $\{N_{i,p}(\xi)\}_{i=1}^{n}$ are defined using a knot vector, which is a non-decreasing sequence of parametric coordinates, written as $\Xi = [\xi_1, \xi_2, \ldots, \xi_{n+p+1}]$, where ξ_i is the ith knot. A knot vector is called open if the first and the last knots both repeat $p+1$ times. Open B-splines are standard in the CAD literature. A knot vector is uniform if all interior knots are equally distributed. Non-uniform and rational B-splines are referred to as NURBS. In this work, the open and uniform knot vectors are considered, which are described in this section. Given a knot vector, the B-spline basis functions are defined recursively starting with piecewise constants ($p = 0$):

$$N_{i,0}(\xi) = \begin{cases} 1, & \text{if } \xi_i < \xi < \xi_{i+1}, \\ 0, & \text{otherwise} \end{cases}$$

The higher order B-splice basis functions ($p \geq 1$) follows from the Cox-de Boor recursion formula:

$$N_{i,p}(\xi) = \frac{\xi - \xi_i}{\xi_{i+p} - \xi_i} N_{i,p-1}(\xi) + \frac{\xi_{i+p+1} - \xi}{\xi_{i+p+1} - \xi_{i+1}} N_{i+1,p-1}(\xi) \tag{2.1}$$

One of the main features of B-spline basis function is that each pth order basis function has $p-1$ continuous derivatives across the knots. In case of knot vectors with repeated interior knots, the basis functions of order p have $p-r_i$ continuous derivatives across the knot with r_i its multiplicity.

In two- and three- dimensional problems, the multivariate B-splines are generated by a tensor product. Surfaces and volumes constructed using multivariate B-splines are referred to as bivariate and trivariate patches. For example, trivariate basis functions defined over the parameter domain $\Omega \in \mathbb{R}^3$ with coordinate $\xi = (\xi, \eta, \zeta)$ are given by:

$$N_A(\xi) = N_i(\xi)N_j(\eta)N_k(\zeta) \tag{2.2}$$

One of the challenges in IGA is that it generally involves multiple trimmed surfaces or curves especially for the complex geometries in engineering design. The conforming IGA framework does not naturally treat these trimmed surfaces or curves. The natural analysis equivalent of trimmed geometries in CAD is enriching the IGA framework with immersed methods, which is discussed in the following section.

2.2   Immersogeometric analysis

The Finite Cell Method (FCM) (detailed in section 1.2), an immersed finite element method introduced by Rank et al. [24], has been found as a natural companion to IGA. In this work, the framework in which IGA is integrated with FCM is considered for flow problems. The use of B-spline basis fucntions in a Finite Cell Method (FCM) was first proposed by Schilinger et al. [32][27][31] and it is referred to as immersogeometric analysis. The framework enables the construction of high-regularity spline spaces on domains of complex geometries. In this framework, the domain of interest is embedded in an ambient regular mesh. The B-spline basis functions are constructed over the structured domain for the trial and test spaces with the Galerkin method. Hierarchical B-splines can be employed for local refinements.

Immersogeometric analysis has been applied to various problems in the fields of solid and structural mechanics [38], fluid mechanics [41, 13], fluid-structure interaction [16] and image-based analysis [33, 39]. Image-based analysis is one of the interesting applications of this framework. An image-based smooth geometry reconstruction from voxel data using a B-spline approximation was introduced by Verhoosel [39].

In the Finte Cell Method, traditional integration methods for the cut-cells (the cells which are intersected by the boundary of the physical domain) are not accurate enough. Verhoosel et al. [39] showed that the accuracy can be improved by implementing a tessellation based quadrature method. This procedure is schematically illustrated in Fig. 2.1. The quadrature construction procedure starts with a multilevel uniform refinement. All cut elements would be refined uniformly until a refinement depth ρ_{max}. The trimmed elements can be identified with the help of a levelset function (derived from the voxel scan data). On regular integration sub-cells, a regular Gauss integration scheme is adopted. On the finest cut elements of level ρ_{max}, a tessellation is conducted with the help of level sets. Gauss quadrature schemes for triangles are employed on triangular elements resulting from this tessellation on the finest integration subcells. The refinement depth is controlled by the integration refinement level ρ_{max}. Details of the method are demonstrated in Fig. 2.1.
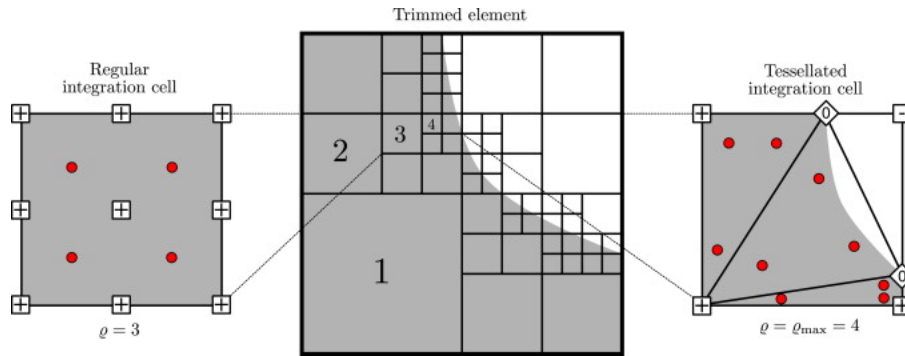
Figure 2.1: A trimmed element is refined up to the level $\rho_{max} = 4$. Evaluation of level sets on on vertices of the integration subcells determines their status. On the left is an example of a regular subcell where 2nd order Gauss quadrature points are marked in red. The right subcell is recognized as a cut-cell due to the negative levelset value. It is triangulated with the help of two zero levelset points. Quadrature points are located in triangles covering the physical domain. Figure from Ref. [39]

Skeleton-based stabilization   For incompressible flow problems, Hoang [10] found that local pressure oscillations occur in the vicinity of cut boundaries (see Fig. 2.2) when the method is employed with inf-sup stable isogeometric element families.
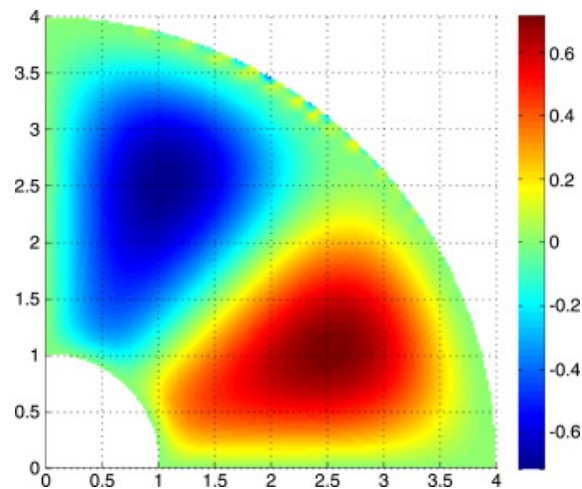

Figure 2.2: Local pressure oscillations in the vicinity of cut boundaries for the Stokes problem with immersogeometric analysis. Image from Ref. [10].

These oscillations can be due to conditioning issues if they occur due to small volume fractions. But, generally, the oscillations occur with relatively large volume fractions. This is a sign of problems related to the inf-sup stability of the discrete problem. By reducing element sizes, global errors vanish and optimal convergence rates can be reached. However, the oscillations in the pressure field persist. Thereby, the compatibility of immersogeometric analysis for incompressible flow problems is severely compromised.

To solve this problem, Hoang et al. [12] proposed a skeleton-based stabilization technique for the incompressible Navier-Stokes problem,

$$\begin{cases} \text{Find} \quad \mathbf{u}^h \in \mathcal{L}(\mathcal{V}^h) \text{and} \quad p^h \in \mathcal{L}(\mathcal{Q}^h), \quad \text{such that for all} (\mathbf{v}, q) \in \mathcal{V}^h \times \mathcal{Q}^h \\ c(\mathbf{u}^h; \mathbf{u}^h, \mathbf{v}^h) + a^h(\mathbf{u}^h, \mathbf{v}^h) + s_{ghost}^h(\mathbf{u}^h, \mathbf{v}^h) + b^h(p^h, \mathbf{v}^h) \quad = l_1^h(\mathbf{v}^h) \\ b^h(q, \mathbf{u}^h) - s_{skeleton}^h(p^h, q^h) \quad = l_2^h(q^h) \end{cases} \quad (2.3)$$

The key idea of this technique is to introduce stabilization terms, which are related to the interface jumps of the highest order derivatives of basis functions in the weak formulation of the mixed problem (Eq. 2.3).

The bilinear and linear operators are defined as in Ref. [12]. The Skeleton-penalty operator (2.5) allows to use identical spaces for the velocity and pressure fields. The Ghost-penalty term (2.4) is added to avoid ill-conditioning of the discretized problem.

$$s_{ghost}^h(\mathbf{u}^h, \mathbf{w}^h) := \sum_{F \in \mathcal{F}_{ghost}^h} \int_F \hat{\gamma} \mu h^{2k-1} [\![\partial_n^k \mathbf{u}^h]\!] \cdot [\![\partial_n^k \mathbf{v}^h]\!] ds \quad (2.4)$$

$$s_{skeleton}^h(\mathbf{u}^h, \mathbf{w}^h) := \sum_{F \in \mathcal{F}_{skeleton}^h} \int_F \gamma \mu^{-1} h^{2k+1} [\![\partial_n^k p^h]\!] \cdot [\![\partial_n^k q^h]\!] ds \quad (2.5)$$
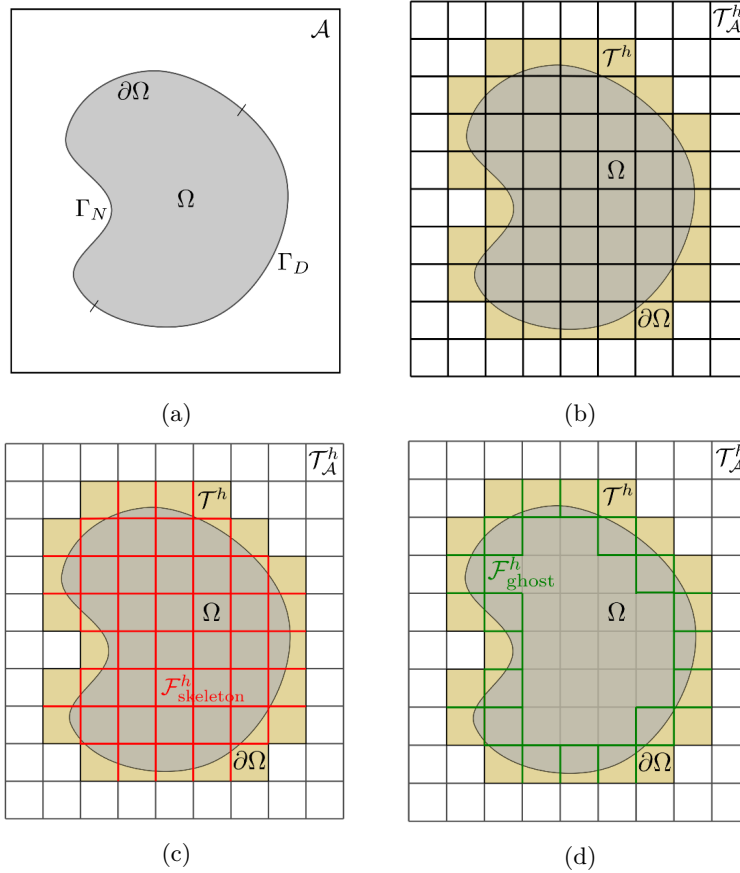

Figure 2.3: Schematic representation for: (a) physical domain Ω embedded in ambient domain $\mathcal{A}$. (b) ambient domain mesh $\mathcal{T}_A^h$ (covering the complete ambient domain) and background mesh $\mathcal{T}^h$ (marked by yellow shading). (c) the skeleton structure. (d) the ghost structure. Figures from Ref. [12]

In the above expressions, μ is the viscosity, γ and $\hat{\gamma}$ are stabilization parameters, $\mathcal{F}^h_{ghost}$ and $\mathcal{F}^h_{skeleton}$ are the ghost structure and the skeleton structure which are defined on the background mesh $\mathcal{T}^h := \{K \in \mathcal{T}^h_{\mathcal{A}} : K \cap \Omega \neq \emptyset\}$ (as shown in Fig. 2.3):

$$\mathcal{F}^h_{skeleton} := \{\partial K \cap \partial K' | K, K' \in \mathcal{T}^h, K \neq K'\} \tag{2.6}$$

$$\mathcal{F}^h_{ghost} := \mathcal{F}^h_{skeleton} \cap \{F | F \subset \partial K : K \in \mathcal{T}^h, K \cap \partial \Omega \neq \emptyset\} \tag{2.7}$$

The jump operator $[\![\cdot]\!]$ in $[\![f]\!]$ refers to the difference between the traces of the function f on the two opposite sides of each face $F \in \mathcal{F}^h_{skeleton}$.

2.3 Problem definition

Thompson in [36] demonstrated that the flow in a Tesla valve is laminar when the Reynolds number is less than 300 at the inlet. For low Reynolds numbers, it is typical to assume steady flow. Therefore, in this work we investigate the Immersogeometric analysis of incompressible Stokes flow (Eq. 2.8) in Tesla valves. We consider the inner area of the channel as domain Ω, the left and right walls (Γ^- and Γ^+) of the channel as the periodic boundary (detailed in the Section 2.4) and the top and bottom wall of the channel as the non splitting Dirichlet boundary Γ_D.

$$\begin{cases} \text{Find} \quad \mathbf{u} : \Omega \to \mathbb{R}^d, \quad p : \Omega \to \mathbb{R} \quad \text{such that,} \\ -2\mu \nabla \cdot (\nabla^s \mathbf{u}) + \nabla p = \quad 0 \quad \text{in} \quad \Omega, \\ \nabla \cdot \mathbf{u} = \quad 0 \quad \text{in} \quad \Omega, \\ \mathbf{u} = \quad 0 \quad \text{on} \quad \Gamma_D, \end{cases} \tag{2.8}$$

where μ represents the dynamic viscosity of the flow and ρ is the density. The formulation (2.8) can be condensed using the stress $\sigma := (-2\mu \nabla^s \mathbf{u} + p\mathbf{I})$ as:

$$\begin{cases} \nabla \cdot (\sigma(\mathbf{u})) = \quad 0 \quad \text{in} \quad \Omega, \\ \nabla \cdot \mathbf{u} = \quad 0 \quad \text{in} \quad \Omega, \\ \mathbf{u} = \quad 0 \quad \text{on} \quad \Gamma_D, \end{cases} \tag{2.9}$$

The implementation of the boundary conditions is details in the next section.

2.4 Periodic boundary conditions

2.4.1 Introduction

The geometry of the multistage T45-R Tesla valve (see Fig.1.2) has a recognizable periodicity. Therefore, the possibility of enforcing the periodic boundary conditions on one of the units of the multistage Tesla valve is investigated in this section. This is non-trivial and novel, especially in the context of immersogeometric analysis.

Various studies in the literature about the influence of the number of stages in the multistage Tesla valve illustrated the suitability of assuming periodicity. Reed and Fla [28] proved with their experiments that increasing the number of Tesla valves from 1 to 2 has significant influence on the flow properties. Further increasing the number of stages leads to increasing pressure difference without obvious influence on the diodicity. Numerical analysis performed by Mohammadzadeh [23] and Thompson [36] validated the independence between the diodicity and the number of stages for the multistage Tesla valves with the Reynolds number less than 50. If the Reynolds number is greater than 50, the diodicity tends to increase with the number of stages until it reaches a certain limitation point. In this work, the Reynolds number is controlled under 50, and therefore the assumption of periodicity can be expected to hold.

Imposing periodic boundary conditions in the Finite Element Method (FEM) is an important topic in, e.g., the computational theory of composite materials. It has been broadly investigated on representative volume elements. The classical approach is to ensure equal values on the matching nodes of the opposite boundaries. This can be achieved by elimination of the degrees of freedom or by application of Lagrange multipliers. However, the classical approach cannot guarantee the alignment of the mesh on the opposite boundaries. This problem was solved by using a master-slave method which was proposed by Yuan [42]. Wang et al. [40] presented a new approach to impose the periodic boundary conditions using the radial point interpolation method.

Weak imposition is another approach of implementing periodic boundary conditions. Larsson et al. [17] introduced a weak formulation by transforming the strong constraints of the periodicity to Neumann boundary conditions. Additionally, Svenning et al. [34] proved the feasibility to use a mixed variational formulation to impose periodic boundary conditions in a weak sense. Reis et al. [29] introduced the formulation to enforce periodic constraints with the mortar discretization and Lagrange multipliers.

Immersogeometric analysis is a non-conformal setting and hence the Dirichlet boundary conditions should be imposed weakly using, e.g., Nitsche's method (which maintains the size of the system of equations and the positive definiteness of the matrix) [30]. This has been employed in a number of studies in the field of isogeometric analysis [5] [9]. However, imposition of the periodic boundary conditions with the Nitsche's method in immersogeometric flow problems has not been explored (up to the author's knowledge).

In this section we implement Nitsche's method to weakly impose the periodic boundary conditions in the immersogeometric analysis of the channel flow problem in Tesla valves. The steady Navier-Stokes problem Eq. (2.8) is considered for the formulation. Unlike in complex unstructured conforming meshes, the mesh distribution on the periodic boundary is easily controlled by virtue of the uniform meshing of the extended domain. Finally, the effectiveness of the proposed method is demonstrated using a prototypical example (see Fig. 2.4).

2.4.2   Description of constraints

The left and right boundary of the domain (Fig. 2.4) are the opposite periodic boundaries Γ_- and Γ_+, where the periodic boundary conditions are to be enforced. The periodic nature of these boundaries is defined by implementing the jump conditions for velocity and pressure at the periodic boundaries as:

$$\begin{aligned}[\![\mathbf{u}]\!] &= 0, \\ [\![p]\!] &= p_0.\end{aligned} \tag{2.10}$$

The jump operator $[\![\cdot]\!]$ is defined as $[\![w(y)]\!] = w(x^+, y_0) - w(x^-, y_*)$, where x^-, x^+ refers to the x-coordinate and y_0, y_* refers to y-coordinate on Γ_+ and Γ_-. Since the opposite boundaries are identical and both of them are parallel to the y axis, the mapping from y_0 to y_* is simple. All other boundaries are considered as non-slipping boundaries denoted by Γ_D, where the Dirichlet condition is imposed ($\mathbf{u} = \mathbf{0}$).

2.4.3   Discretization and Nitsche's method

In order to incorporate the homogeneous periodic constraints, the pressure is divided into two parts as: $p = \tilde{p} + \hat{p}$. A lift term $\hat{p} = p_0 \cdot \frac{x}{L}$ is extracted to eliminate the pressure drop between the opposite boundaries. The $\tilde{p}$ term enforces the periodic constraint. The stress now can be written as:

$$\sigma = (-2\mu\nabla^s\mathbf{u} + \tilde{p}\mathbf{I}) + \hat{p}\mathbf{I} = \tilde{\sigma} + \hat{p}\mathbf{I}. \tag{2.11}$$
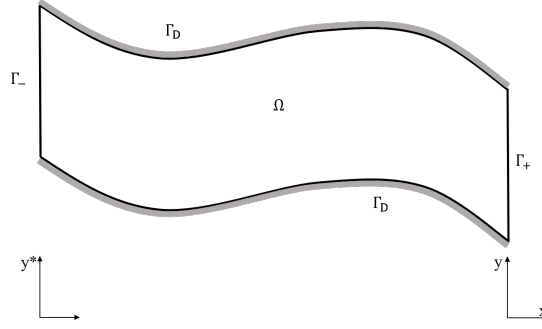
Figure 2.4: Geometry of a prototypical channel segment with constraints

The velocity and pressure fields are discretized using the Galerkin method. The trial and test function spaces for velocity and pressure are defined as:

$$\mathcal{V}_{0,f} = \left\{ \mathbf{u} \in \mathcal{H}^1(\Omega) : \mathbf{u} = \mathbf{0} \quad \text{on} \quad \Gamma_{wall}, \quad \mathbf{u} = \mathbf{f} \quad \text{on} \quad \Gamma_{in} \right\} \tag{2.12}$$

$$\mathcal{Q} = \left\{ \mathcal{L}^2(\Omega) \right\} \qquad \mathbf{v} \in \mathcal{V}_{0,0} \qquad \mathbf{q} \in \mathcal{Q} \tag{2.13}$$

The space $\mathcal{H}^1$ refers to the first-order Sobolev space, which is a space of functions which are bounded in the following norm:

$$||\phi||^2_{H^1(\Omega)} = ||\phi||^2 + ||\nabla\phi||^2 \tag{2.14}$$

The $\mathcal{L}^2$ is a space of integrable real-valued functions $\phi : \Omega \to \mathbb{R}$ for which the following norm (or integral) is bounded:

$$||\phi||^2_{L_2(\Omega)} = \int_\Omega \phi^2 d\Omega \tag{2.15}$$

The weak form of the incompressible steady Navier-Stokes problem (2.9) is:

$$-\int_\Omega \tilde{\sigma} : \nabla\mathbf{v} d\Omega + \int_\Gamma (\tilde{\sigma} \cdot \mathbf{n}) \cdot \mathbf{v} d\Gamma + \int_\Omega \nabla\hat{p} \cdot \mathbf{v} = 0 \tag{2.16}$$

Since $\nabla \cdot \mathbf{u} = 0$ on Ω, Eq. 2.16 leads to :

$$-\int_\Omega \tilde{\sigma} : \nabla\mathbf{v} d\Omega - \int_\Gamma (\tilde{\sigma} \cdot \mathbf{n}) \cdot \mathbf{v} d\Gamma - \int_\Omega \nabla\hat{p} \cdot \mathbf{v} - \int_\Omega q\nabla \cdot \mathbf{u} = 0 \tag{2.17}$$

The integration on boundaries can be re-formulated to include the periodic conditions:

$$-\int_{\Gamma_D \cup \Gamma_+ \cup \Gamma_-} (\tilde{\sigma} \cdot \mathbf{n}) \cdot \mathbf{v} d\Gamma = -\int_{\Gamma_D} (\tilde{\sigma} \cdot \mathbf{n}) \cdot \mathbf{v} d\Gamma - \int_{\Gamma_+} (\tilde{\sigma_+} \cdot \mathbf{n}_+) \cdot \mathbf{v}_+ d\Gamma$$

$$-\int_{\Gamma_-} (\tilde{\sigma_+} \cdot \mathbf{n}_-) \cdot \mathbf{v}_- d\Gamma - \int_{\Gamma_-} ((\tilde{\sigma_-} - \tilde{\sigma_+}) \cdot \mathbf{n}_-) \cdot \mathbf{v}_- d\Gamma$$

$$= -\int_{\Gamma_D} (\tilde{\sigma} \cdot \mathbf{n}) \cdot \mathbf{v} d\Gamma - \int_{\Gamma_+} (\tilde{\sigma_+} \cdot \mathbf{n}_+) \cdot (\mathbf{v}_+ - \mathbf{v}_-) d\Gamma$$

$$= -\int_{\Gamma_D} (\tilde{\sigma} \cdot \mathbf{n}) \cdot \mathbf{v} d\Gamma - \int_{\Gamma_+} (\tilde{\sigma_+} \cdot \mathbf{n}_+) \cdot [\![\mathbf{v}]\!] d\Gamma$$

Identical order spline basis functions are considered for the discretization of the velocity and the pressure fields:

$$\mathcal{V}^h = \left[\mathcal{S}_\alpha^k\right]^d \cap \mathcal{V}_{0,f} \qquad \mathcal{Q}^h = \mathcal{S}_\alpha^k \cap \mathcal{Q} \tag{2.18}$$

$\mathcal{S}_\alpha^k$ refers to the space of spline basis functions of degree k and regularity α. In the example considered in this section, second order splines are considered ($k = 2$). The formulation to impose the Dirichlet boundary and the periodic boundary conditions using Nitsche's method is proposed as the following:

$$\int_\Omega \tilde{\sigma}(\mathbf{u}^h) : \nabla\mathbf{v}d\Omega - \int_\Omega \nabla\hat{p} \cdot \mathbf{v} - \int_\Omega \nabla \cdot \mathbf{u}^h \cdot q-$$

$$\int_{\Gamma_D} (\tilde{\sigma}(\mathbf{u}^h) \cdot \mathbf{n}) \cdot \mathbf{v}^h d\Gamma - \int_{\Gamma_D} (\tilde{\sigma}(\mathbf{v}^h) \cdot \mathbf{n}) \cdot \mathbf{u}^h d\Gamma + \int_{\Gamma_D} \frac{\mu\beta}{h}\mathbf{u}^h \cdot \mathbf{v}^h d\Gamma-$$

$$\int_{\Gamma_+} (\tilde{\sigma}(\mathbf{u}^h) \cdot \mathbf{n}) \cdot [\![\mathbf{v}^h]\!]d\Gamma - \int_{\Gamma_+} (\tilde{\sigma}(\mathbf{v}^h) \cdot \mathbf{n}) \cdot [\![\mathbf{u}^h]\!]d\Gamma + \int_{\Gamma_+} \frac{\mu\beta}{h}[\![\mathbf{u}^h]\!] \cdot [\![\mathbf{v}^h]\!]d\Gamma = 0, \tag{2.19}$$

where h is the element size and β is a stabilization parameter which is scaled by the viscosity μ. In this study, a global β is used and the appropriate values are yet to be discussed. The terms in the second and third lines of equation (2.19) are the Nitsche terms [15]. It contains three terms: the first term is coercive, the second term maintains the symmetry, and the third term is for the stabilization.

2.4.4 Periodic point association

Typical approaches for the weak enforcement of periodic boundaries contain complex point projections to accomplish the integration of jump terms on opposite boundaries with an un-matching mesh. This disadvantage is ameliorated in this study by virtue of the immersed method.

For any given geometry, the Finite Cell Method starts with embedding the domain in a rectangular ambient grid. The cut-cells (cells containing the boundary) undergo multilevel refinement based on refinement indicator (see Fig. 2.5b). In this scenario, the main idea to implement periodic boundary conditions is to specify the axis of the boundary where periodic conditions are to be imposed, for example y_1 and y_2 (as shown in Fig. 2.5a). The distance between these two axes is evaluated as $\Delta y = y_2 - y_1$ and the number of elements n to divide the boundary is defined.

In this way, an ambient mesh with size of $h = \frac{\Delta y}{n}$ is generated and it is symmetric about the axis of opposite periodic boundaries. Therefore, refinement using the strategy described in Fig. 2.1 results in identical trimmed elements on the opposite periodic boundaries. The integration of the jump term is evaluated by the accumulation of element-wise differences of the function on opposite boundaries:

$$\int_{\Gamma_+} [\![f^h]\!]d\Gamma \approx \Sigma_{\mathcal{F}_i \in \Gamma_+}(f_i^* - f_i) \tag{2.20}$$

By controlling the size and offset of the ambient mesh, the periodic boundaries are trimmed equally and hence complex projection techniques are avoided.
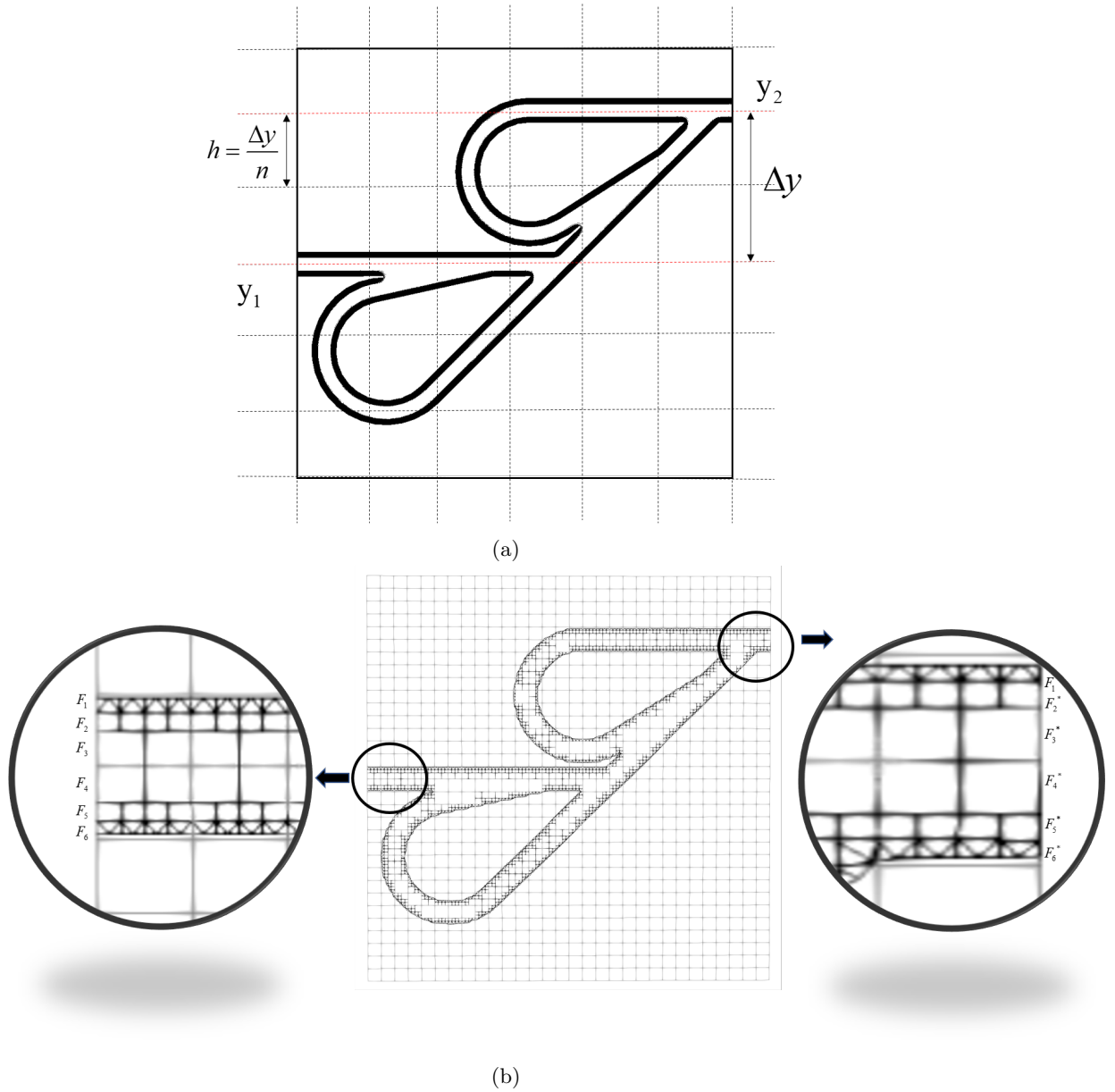
(a)

(b)

Figure 2.5: (a) Generated ambient mesh of size h on axis of periodic boundaries. (b) Identical trimmed elements on periodic boundaries

2.5 Prototypical test case

In this section we present a test case to demonstrate the Nitsche's method to weakly impose the periodic boundary conditions in the immersogeometric analysis. The Stokes flow problem Eq. 2.8 in a channel of a simple valve (see Fig. 2.4) is considered for this study.

The first step of the simulation is to scan the geometry from the image using the image-based analysis proposed in [39]. Following the immersed method, the physical domain is embedded in the extended mesh and B-spline bases are employed for the discretization of the ambient domain. The integration is conducted on the trimmed domain, with multilevel refinements (defined using a refinement indicator) and the tessellation method as described in Fig. 2.1.

The values for the density ρ and the dynamic viscosity μ of the flow are assigned by assuming water flow at room temperature, that is $\rho = 10^3 \quad kg/m^3, \mu = 10^{-3} N \cdot s/m^2$. The periodic boundary condition is weakly imposed using the Nitsche's method as proposed in Sec. 2.4. The influence of the Nitsche's parameter β in Eq. 2.19 on the performance of the method will be discussed in later sections. The skeleton-based stabilization method in Sec. 2.2 is implemented to avoid oscillations. The sensitivity to the skeleton and the ghost parameter γ in Eq. 2.5, Eq. 2.4 is yet to be investigated.

The velocity and the pressure fields of the Navier-Stokes problem, with stabilization parameter $\beta = 100$, are shown in Fig. 2.6. The color mapped from the magnitude of the velocity changes from red to blue suddenly in the normal direction of the wall, which demonstrates no slip condition at the wall. The imposed pressure difference between the inlet and the outlet is very obvious in the color map. The velocity and pressure fields demonstrate the recognizable periodicity.
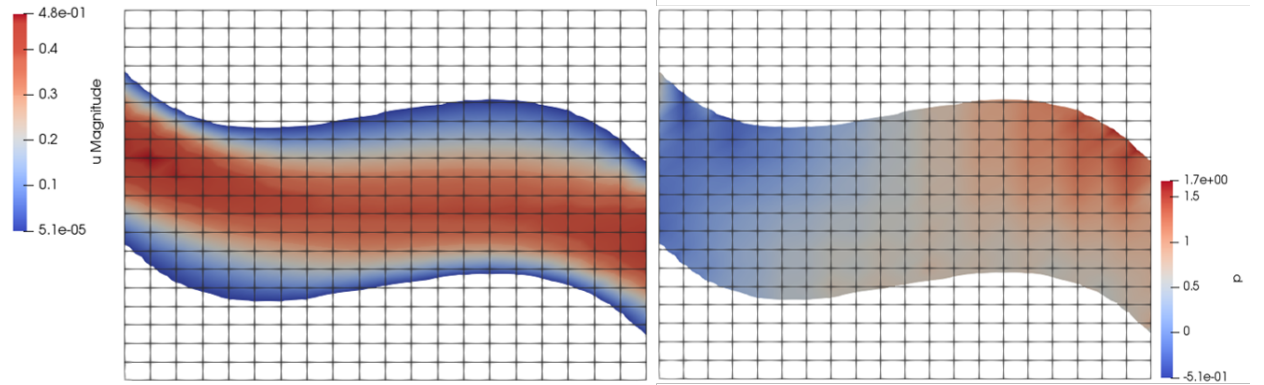

Figure 2.6: Velocity and pressure fields of the Stokes problem (Eq. 2.8)

In Fig. 2.7, we study the influence of the mesh size h and the Nitsche's parameter β on the convergence behavior of the jump of velocity for the proposed method. Here, the second order B-spline basis functions ($k = 2$) are employed. The differences of velocity on opposite boundaries are evaluated element-wise, which is feasible with the offset method introduced in Sec. 2.4.4. A study is conducted with background meshes varying from 20×20 elements to 120×120 elements. The default value of β is set to 100. The $\mathcal{L}^1$ norm of the jump velocity on opposite boundaries is shown in Fig. 2.7a from which we observe that it converges at a rate of 4. Different cases with the varying Nitsche's parameter β (ranging from 50 to 2000) and with 50×50 elements are studied. We observed that the $\mathcal{L}^1$ norm of the jump velocity converges at a rate of 1.5 with increasing β (see Fig. 2.7b). A relatively large value of β is beneficial for the imposition of the periodic boundary condition. The convergence behavior of the jump velocities demonstrates the proper imposition of the periodic boundary conditions. The $\mathcal{L}^1$ norm of the jump velocity is under 10^{-4} for $\beta = 100$ and for meshes consist 50×50 elements. This setting will be considered as the default setting for later simulations.
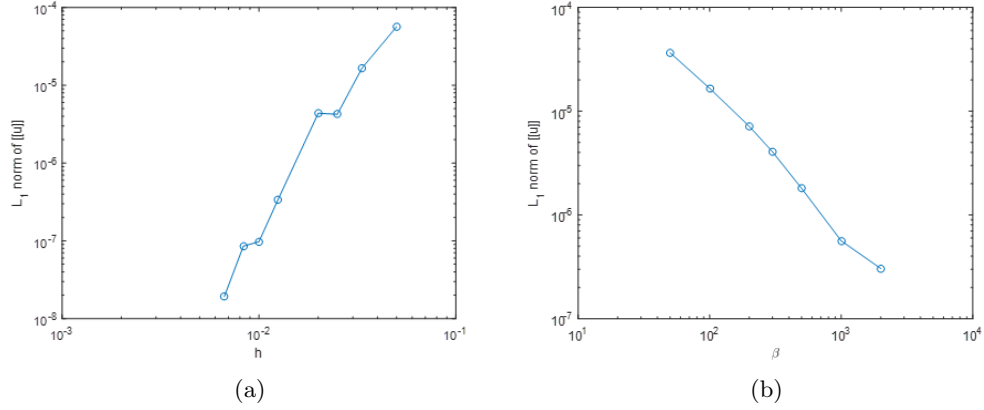
(a)   (b)

Figure 2.7: Convergence of the jump velocity for different element sizes h and Nitsche's parameters β.

In Fig. 2.8, we study the h-convergence behavior of the proposed method for B-spline basis functions of orders $k = 2, 3$. Again, a study is conducted with background meshes varying from 20×20 elements to 150×150 elements. The Nitsche's parameter $\beta = 100$ is considered, $\gamma = 0.1$ is assigned to both the skeleton and ghost parameter. The flux $\int \mathbf{u} \cdot \mathbf{n}$ is evaluated at the left and the right boundary and the average value is recorded. The flux with the finest mesh (150×150) is chosen to be the reference. For different mesh sizes h, the flux is compared with this reference and the convergence of the relative error is studied. The behavior of the convergence is not of any obvious pattern. The uniqueness of the solution for Stokes problem with periodic boundary conditions has been proved in [2]. One possible reason is that errors are involved when the geometry is reconstructed with the image based immersed method. Refinement of the ambient mesh does not help to eliminate errors rooted in the voxel representation of the geometry, especially of the opposite boundaries. Exact explanation remains to be investigated. In addition, the increase of the degree of the B-spline basis functions does not have apparent influence on the behavior of convergence.
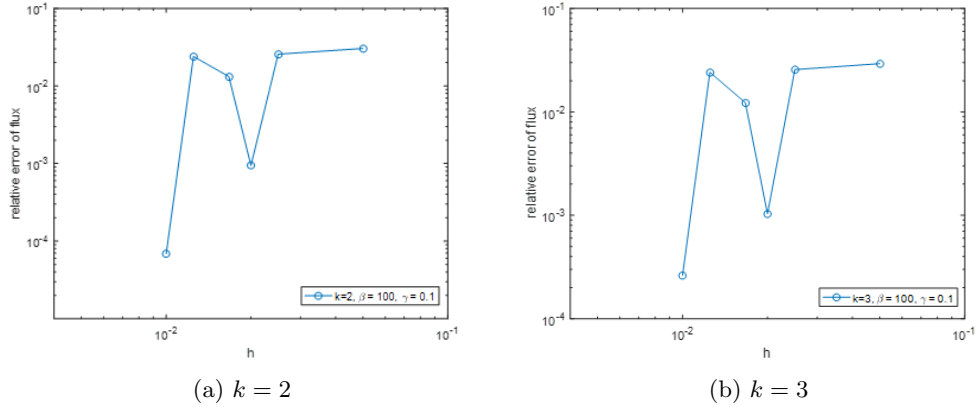

(a) $k = 2$ (b) $k = 3$

Figure 2.8: Convergence of the relative error of flux for different element sizes h.

In Fig. 2.9, we study the h-convergence behavior of the proposed method for B-spline basis functions of order $k = 2, 3$. The mesh consists of 50×50 elements. $\gamma = 0.1$ is assigned to both the skeleton and ghost parameter. The Nitsche's parameter β is chosen from a set of values from 100 to 1000. The relative error of flux is evaluated with the same method described before. For the relative error of flux, asymptotic rates (around 0.5) are obtained. Similar to the previous study,

the order of the B-spline basis functions does not have obvious influence on the flux.
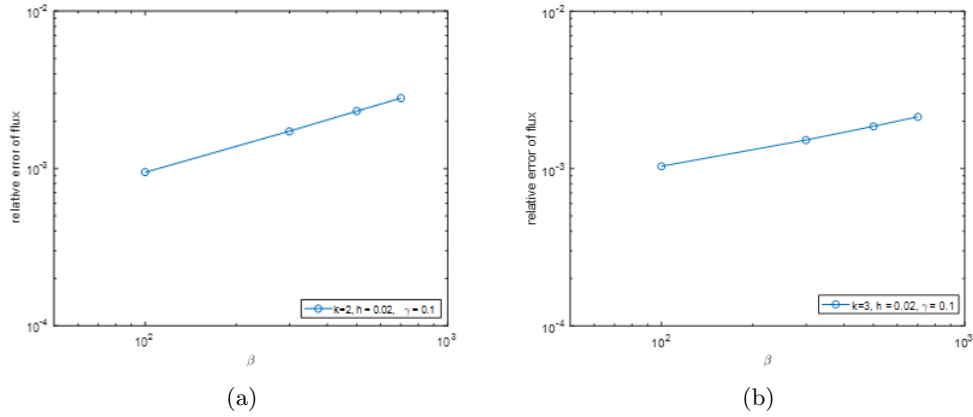

(a)   (b)

Figure 2.9: Convergence of the relative error of flux for different Nitsche's parameter β for (a) $k = 2$, (b) $k = 3$.

In Fig. 2.10 we study the sensitivity of the proposed method to the skeleton and ghost parameter in Eq. 2.5. Meshes with 50×50 elements and the B-spline basis functions of order $k = 2$ and the Nitsche's parameter $\beta = 100$ are considered. The skeleton and ghost parameter are always assigned with identical values. As shown in Fig. 2.10, larger values of γ always results in larger relative errors of the flux. When $h \approx h_0 = 0.016$, the relative errors are similar for different values of γ. When h increases from h_0 or when h decreases from h_0, the influence of the parameter γ becomes more significant.

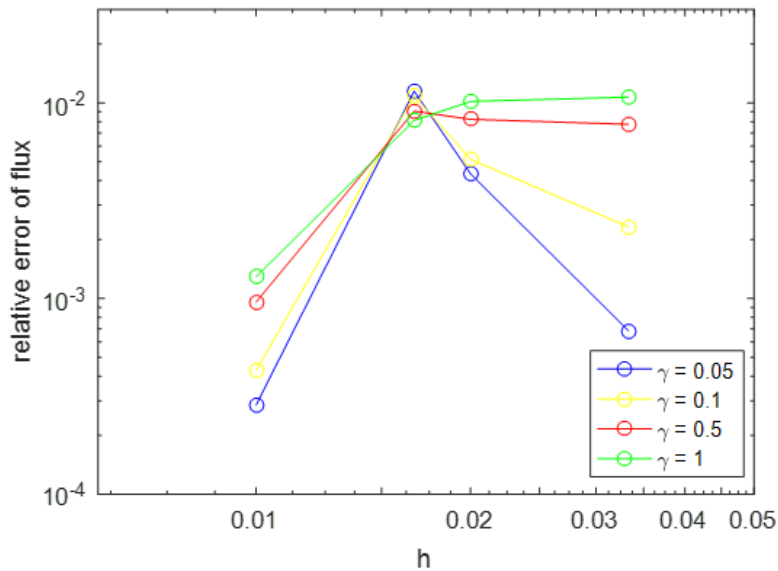
Figure 2.10: Convergence of the relative error of flux for different skeleton parameters γ.

Chapter 3

CAD-based immersogeometric analysis

In the previous chapters, the image-based immersed isogeometric method has been studied and adapted for the analysis of the flow in Tesla valves. For an idealized design-through-analysis workflow (which includes geometry reconstruction and implementation of the numerical method), a CAD model instead of images or voxel data should be at the starting point of the analysis workflow.

In this chapter, the prototype of a workflow where CAD models are taken as inputs and numerical analysis results are given as outputs, is proposed. Section 3.2 provides an introduction to common data exchange formats. Next, in Section 3.3 a levelsets based geometry reconstruction method is proposed, including approaches to generate levelset functions directly from the CAD data and strategies for further smoothing. Then, the constructed geometry is employed to conduct an immersogeometric analysis. Section 3.4 finally illustrates the extension of the workflow to three dimensional problems and gives an idea about how the workflow can be simplified using CAD-based immersogeometric analysis compared to traditional methods used in industries.

3.1   Data exchange formats

CAD models in different systems are based on different data formats. Before discussing the geometry reconstruction from data files of CAD models, it is helpful to have an overview of the most prominent data exchange formats, namely the Initial Graphics Exchange Specification (IGES) and the Standard for The Exchange of Product (STEP) model data. Data files of CAD models contain much information, including parameters, constraints, features and design histories. For numerical analysis, only specific information is significant, i.e., the geometry and the topology (addressed in detail in the next section). In this section we provide background of the CAD data file formats used in this work.

3.1.1   IGES

IGES is a neutral data format and was developed by the U.S. National Bureau of Standards in 1980. In 1991, the fifth version, also the latest version of IGES was produced, supporting wireframes, freeform surfaces and boundary representations of solids. The IGES format is based on ASCII standard code and can be divided in 5 separate segments, appearing in sequence:

1. START

2. GLOBAL

3. DATA ENTRY

4. PARAMETER DATA

5. TERMINATE

The START and the GLOBAL sections contain the name of the file and its sources, the delimiters for the Parameter Data section, the author of the file, and other general information. The strings are in Hollerith format, each one with the number of characters it contains followed by an H preceding it.

Entity Type	PD pointer	Structure	Line Font Pattern	Level	View	Transformation matrix pointer	Label Display Associativity	Status Number	Section Code and Sequence Number
Entity Type	Line Weight Number	Color Number	Parameter Line Count	Form Number	Reserved	Reserved	Entity Label	Entity Subscript Number	Section Code and Sequence Number

Figure 3.1: Fields of the DATA ENTRY section in one line. Fields marked in red are important for the extraction of the boundary information.

The basic unit of data in the IGES format is an entity. There are 150 types of entities in IGES. The DATA ENTRY section lists all entities of the file. An example of one line in the DATA ENTRY is shown in Fig. 3.1. The entity type is a three digit number starting from 100 which is unique for different types of entities. The PD pointer provides the reference to the specific entity in the PARAMETER DATA section. The Sequence Number starts with 'D' and consists of the line number for this section. The Parameter Line Count refers to the number of lines this entity takes in the PARAMETER DATA section.

3.1.2 STEP

STEP stands for the standard officially denoted as ISO 10303. The first part of it was released in 1994 and it is undergoing continuous development, including recent enrichments to better support isogeometric analysis. The development of STEP is based on three principles:

1. Encompassing data relevant to the entire life cycle of a product including design, manufacturing, quality, testing and support.

2. Storing data in an application layer separated from the generic shape information.

3. Utilizing a formal language to describe the data structure.

A STEP file is organized in 2 sections, "HEADER" and "DATA", both terminated by "ENDSEC". The HEADER section consists of FILE_DESCRIPTION, FILE_NAME and FILE_SCHEMA. These are equivalent to the START and GLOBAL sections of the IGES format.

The DATA sections in STEP files are described in a language named EXPRESS following the principle 3. In EXPRESS, an object is abstracted to an ENTITY and a collection of entities is a SCHEMA. Each entity instance has a unique mark, which is a positive number preceded by a hashtag " # NUMBER ". The mark is used as a reference to this entity in the file. Each line in DATA stands for an entity:

$$\#NUMBER = ENTITY\_NAME(Attribution\_1, Attribution\_2, ...) \tag{3.1}$$

Detailed comparisons between different data exhcange formats have been conducted. A recent summary can be found in [20]. Compared with IGES, STEP is superior for its advantages such as

its formal information model. In addition, nowadays STEP is more broadly applied and is in constant development, including further extensions for isogeometric modeling capabilities. Therefore, STEP is the first choice as the information transmitter for the design through analysis workflow. IGES is also considered to demonstrate the compatibility of the proposed workflow.

3.2 Geometry reconstruction from IGES/STEP

In the typical image-based immersed isogeometric analysis setting of Verhoosel et al. [39], grey scale voxel data is approximated by B-spline level set functions. When starting from a CAD model instead of an image, a natural idea is to use a sign function g_1 as the levelset function, which represents whether a point lies inside the boundary of the model or not.

$$g_1(\mathbf{x}) = \begin{cases} -1 & \mathbf{x} \in \Omega_{outside} \\ 0 & \mathbf{x} \in \Gamma \\ 1 & \mathbf{x} \in \Omega_{inside} \end{cases} \qquad (3.2)$$

In this section, the extraction of the boundary information from CAD data files is discussed first. Then approaches to generate levelset values from boundaries are presented. Finally, B-spline approximations to levelset functions are introduced.

3.2.1 Extraction of geometric data from IGES/STEP formats

For boundary representations of models, the extraction process of boundary information from IGES files and STEP files are similar. In both formats, geometries are organized as collections of entities.

For IGES, commonly utilized entities include the Line (Type 110), the Rational B-spline Curve (Type 126), etc. Fields related to these entities are presented in Fig. 3.2 and Fig. 3.3. Once an IGES file is read, the DATA ENTRY list is checked line by line and the corresponding entity in the PARAMETER DATA section can be accessed with the help of the PD pointer. Information in these entities, such as coordinates of the start and the end points for a line, and knot values and control points of a spline, can then be easily extracted.

index	1	2	3	4	5	6
field	x coordinate of start point	y coordinate of start point	z coordinate of start point	x coordinate of end point	y coordinate of end point	z coordinate of end point

Figure 3.2: Fields of LINE entity in IGES files

index	1	2	3	4	5	6
field	Upper index of sum	degree of basis function	flag (planar or not)	flag (open or close)	flag (rational or not)	flag (periodic or not)
index	7	8	9		10	11
field	knot values	weights	coordinates of control points		parameter values	unit normal

Figure 3.3: Fields of SPLINE entity in IGES files

For STEP, a B-spine surface can be divided into a BSPLINE_SURFACE_WITH_KNOTS entity and a collection of several FACE_BOUND entities.

Further splitting leads to BSPLINE_CURVE_WITH_KNOTS entities, with explicit attributions including a list of control points and a list of knot values. Fig. 3.4 provides a comprehensive overview of the structure of a B-spline surface in STEP.
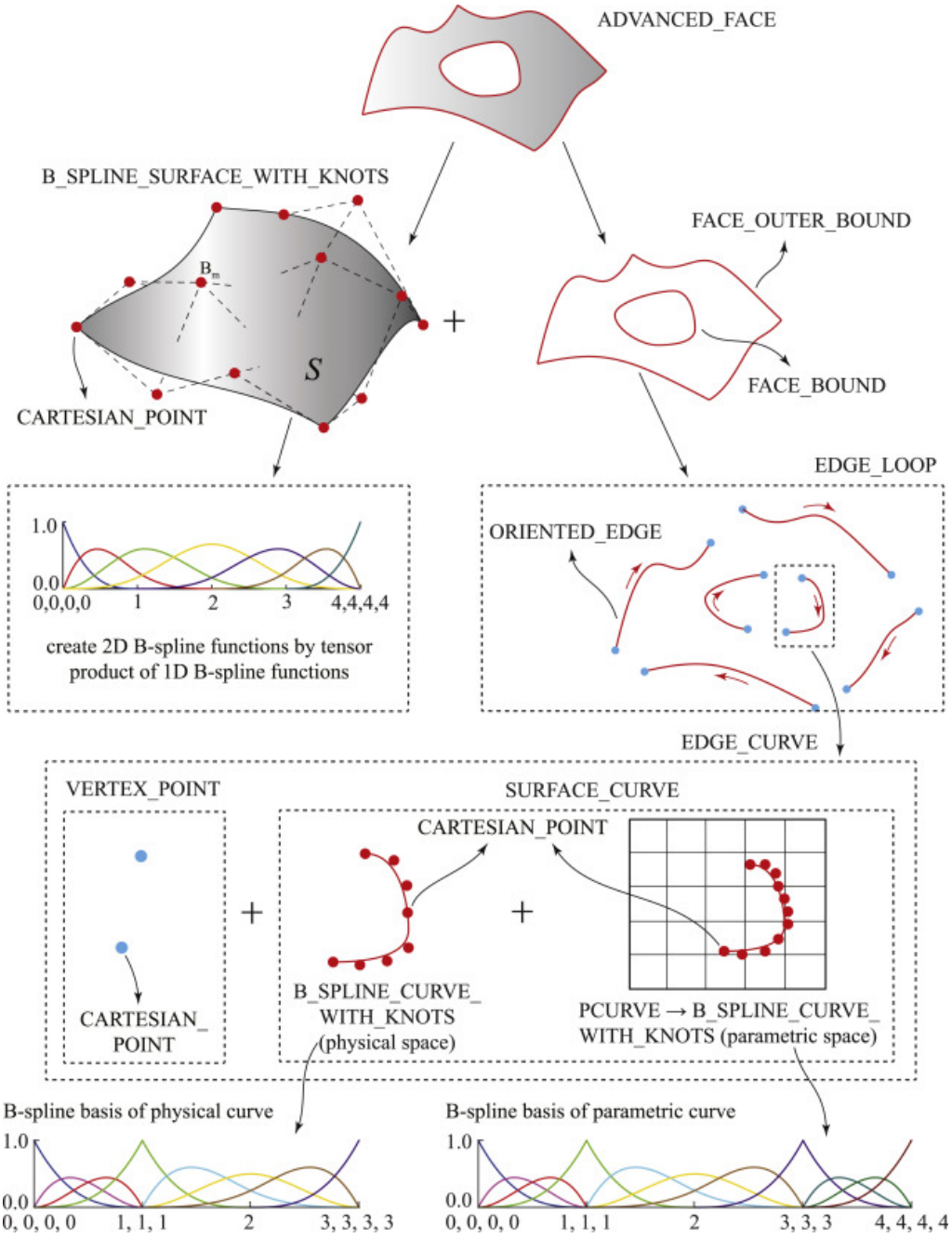

Figure 3.4: The topology and geometry for the boundary representation of a surface in STEP. Image from Ref. [8]

.

3.2.2 Evaluation of levelset functions

For a two dimensional geometry, the boundary of a model is supposed to consist of a set of closed B-splines. A query point is inside the model if it is inside one closed B-spline and outside all other closed B-splines, as exemplified in Fig. 3.5. In Fig. 3.5 $\overrightarrow{A_1 P_1} \cdot \overrightarrow{A_1 B_1} \leq 0$ and $\overrightarrow{A_3 P_1} \cdot \overrightarrow{A_3 B_3} \leq 0$, hence the point P_1 is outside the spline S_1 and outside the spline S_2. Therefore, P_1 is located outside the domain Ω. $\overrightarrow{A_2 P_2} \cdot \overrightarrow{A_2 B_2} \geq 0$ and $\overrightarrow{A_4 P_2} \cdot \overrightarrow{A_4 B_4} \leq 0$, the point P_2 is inside the spline S_1 and outside the spline S_2. Therefore, P_2 is located inside the domain Ω. Similarly, the point P_3 is inside the spline S_1 and inside the spline S_2, thus outside the domain Ω.
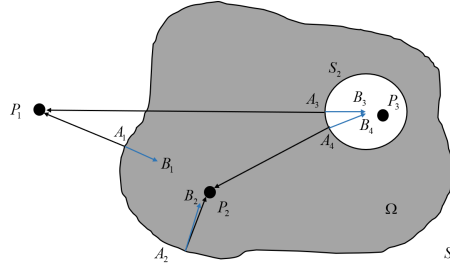
Figure 3.5: Example of a 2D boundary representation of a model with spline boundaries.

Evaluation of the levelset function g_1 (3.2) is equal to the determination of the location of an arbitrary point. To determine the state of an arbitrary point, a general approach is to first find the projection of the point on the contour. Then compare the vector from the query point to the projection, to the normal vector of the curve at the projection point. While the way to conduct the location query is straightforward, the signed distance function from the projection point to the contour can also be obtained in addition to the location state. The signed distance function g_2 is then an alternative for the levelset function.

$$g_2(\mathbf{x}) \begin{cases} < 0 & \mathbf{x} \in \Omega_{outside} \\ = 0 & \mathbf{x} \in \Gamma \\ > 0 & \mathbf{x} \in \Omega_{inside} \end{cases} \tag{3.3}$$

For a closed B-spline, the projection can be found after subdividing the B-spline into a set of Bezier splines. The algorithm for projecting a point on a Bezier spline can be summarized as:

Algorithm 1 Point projection on a Bezier curve

Input: Query point, $P(x, y)$; Bezier spline (knots and control points) B_i;
Output: Closest point P_i to the query point P on curve B_i;
1: Check if the Bezier spline is simple. If so, continue; else do 5,
2: Check if one of the end points is the closest point. If so, return; else, continue;
3: Check if the Bezier spline is flat enough. If so, do 4; else do 5,
4: Approximate the curve with a line segment and conduct the projection
5: Subdivide B_i into two halves B_{2i} and B_{2i+1}. Compare the outputs of algorithm 1 when B_{2i} and B_{2i+1} are inputs and return the closest one.
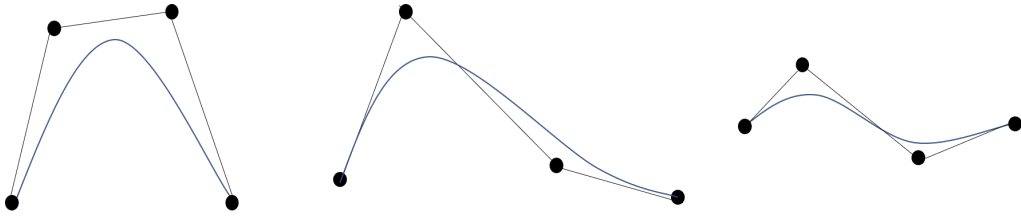

Figure 3.6: Different 2D Bezier splines. A Bezier spline is simple if the control polygon is convex and simple. The first spline is simple, while the second polygon is not convex and the third polygon is not simple.
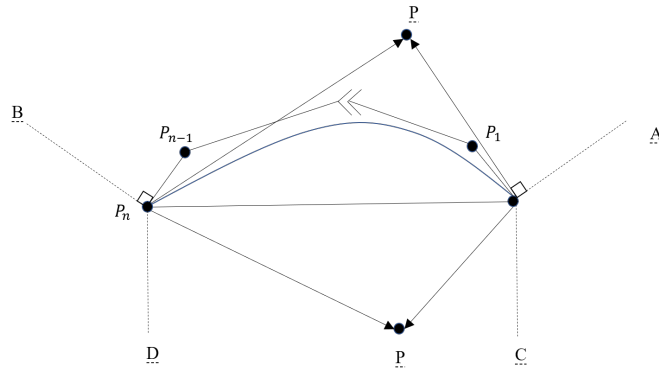

Figure 3.7: When end points are closest to the query point on a Bezier spline, define four dot products $R_1 = \overrightarrow{P_0 P} \cdot \overrightarrow{P_0 P_1}$, $R_2 = \overrightarrow{P P_n} \cdot \overrightarrow{P_{n-1} P_n}$, $R_3 = \overrightarrow{P_n P_0} \cdot \overrightarrow{P_n P}$, $R_4 = \overrightarrow{P_n P_0} \cdot \overrightarrow{P_0 P}$. If either $R_1 < 0$ or $R_2 < 0$, and $R_3 \cdot R_4 > 0$, the nearest point to the query point on the curve must be one of the endpoints.

A simple Bezier spline in Step 1 is defined as a Bezier spline where the control polygon is simple and convex, as shown in Fig. 3.6. A polygon is simple if it is a flat shape consisting of straight, non-intersecting line segments or edges that are joined pair-wise to form a closed path. Step 2 can be implemented by evaluation of several vectors, as shown in Fig. 3.7. A simple Bezier spline is flat if the height-width ratio of its bounding box is below a specified tolerance. More details of the algorithm can be found in YingLiang Ma et al. [19]. Basic operations of splines like subdivision can be found in Piegl et al. [26].

The levelsets g_1 and g_2 for the geometry of a prototypical channel are shown in Fig. 3.8. The levelsets produced by location states coarsely represent the geometry while the levelsets produced by signed distances are considerably more smooth.

Figure 3.8: Original geometry (left), the sign function (middle) and the signed distance function (right) as levelset functions

3.2.3 Bspline level set function

Levelset functions produced by location query lack accuracy to represent the geometry, as illustrated in Fig. 3.8. To get a more smooth levelset function f, the levelsets g_3 can be approximated by Eq. 3.4, where a_i are levelset coefficients and $N_{i,p}$ are B-spline basis functions of order p, defined as the tensor product functions of the univariate open B-spline; see reference [39]. This spline based levelset function resulting from the location query is illustrated in Fig. 3.9. The image after convolution is much more smooth compared with Fig. 3.8 and is, as a matter of fact, close to the original geometry.

$$f(\mathbf{x}) = \sum_{i=1}^{n} N_{i,p}(\mathbf{x})a_i \tag{3.4}$$

$$a_i = \frac{\int_\Omega N_{i,p}(\mathbf{x})g(\mathbf{x})d\mathbf{x}}{\int_\Omega N_{i,p}(\mathbf{x})d\mathbf{x}} \tag{3.5}$$

| (a) | (b) |
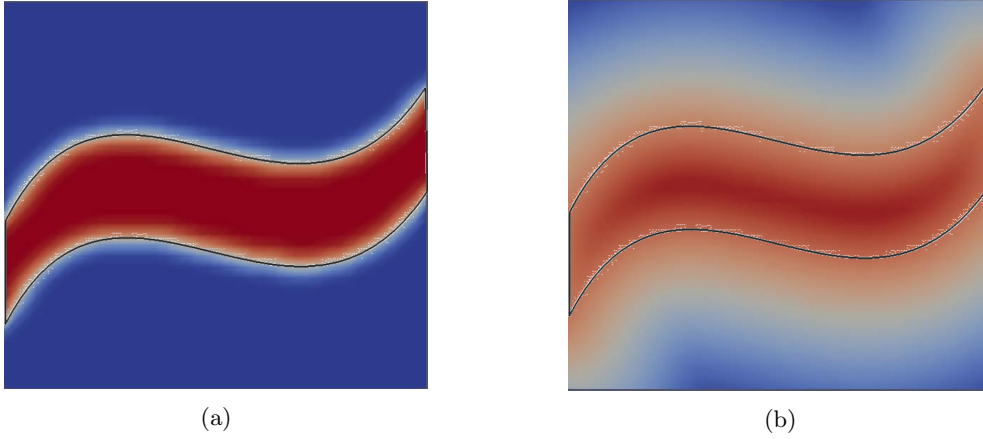
Figure 3.9: B-spline approximation of the sign function (left), the signed distance function (right) as levelset functions. Black curves represent the exact boundary.

3.3 Immersogeometric analysis

Starting from data files in IGES or STEP, smooth levelset values have been obtained after evaluation and convolution. The next step in our work flow is to conduct the immersogeometric analysis described in Chap. 2.

The Navier-Stokes problem for steady incompressible flow is studied here for the flow in a curved channel. The Navier-Stokes equations for the velocity field $\mathbf{u} : \Omega \to \mathbb{R}^d$ and pressure field $p : \Omega \to \mathbb{R}^d$ read:

$$\begin{cases} \text{Find} \quad \mathbf{u} : \Omega \to \mathbb{R}^d, \quad p : \Omega \to \mathbb{R} \quad \text{such that,} \\ \rho\nabla \cdot (\mathbf{u} \otimes \mathbf{u}) - \mu\nabla \cdot (\nabla^s\mathbf{u}) + \nabla p = \quad 0 \quad in \quad \Omega, \\ \nabla \cdot \mathbf{u} = \quad 0 \quad in \quad \Omega, \\ \mathbf{u} = \quad \mathbf{g} \quad on \quad \Gamma_D, \\ 2\mu\nabla^s\mathbf{u} \cdot \mathbf{n} - p\mathbf{n} = \quad 0 \quad on \quad \Gamma_{out}, \end{cases} \tag{3.6}$$

The density and the viscosity of the flow are assigned properties of liquid water at room temperature, $\rho = 10^3 \quad kg/m^3$ and $\mu = 10^{-3}N \cdot s/m^2$. The boundary $\partial\Omega$ consists of Γ_{wall}, Γ_- and Γ_+. For a flow in the positive direction, Γ_- is also Γ_{in} and Γ_+ is Γ_{out}. Γ_{wall} is subject to Dirichlet boundary conditions where velocities are set to zero. A parabolic horizontal velocity profile $\mathbf{f}$ is

imposed on Γ_{in} and Γ_{out} is subject to a homogeneous Neumann boundary condition as indicated in Fig. 2.4. Γ_{in} and Γ_{wall} are combined as Γ_D and a function g is defined on Γ_D such that

$$\mathbf{g} = \begin{cases} \mathbf{0}, & \text{on} \quad \Gamma_{wall}, \\ \mathbf{f}, & \text{on} \quad \Gamma_{in} \end{cases} \tag{3.7}$$

In Eq. 3.6, $\mathbf{n}$ denotes the outward-pointing unit normal vector to $\partial\Omega$.

The velocity space is defined as $\mathcal{V}_f = \left\{ \mathbf{u} \in \mathcal{H}^d(\Omega) : \mathbf{u} = \mathbf{0} \quad \text{on} \quad \Gamma_{wall}, \mathbf{u} = \mathbf{f} \quad \text{on} \quad \Gamma_{in} \right\}$ and $\mathcal{Q} = \left\{ \mathcal{L}^2(\Omega) \right\}$. The velocity test function is defined on a homogeneous space:

$$\mathcal{V}_0 = \left\{ \mathbf{u} \in \mathcal{H}^d(\Omega) : \mathbf{u} = \mathbf{0} \quad \text{on} \quad \Gamma_{wall}, \mathbf{u} = \mathbf{0} \quad \text{on} \quad \Gamma_{in} \right\}$$

The pressure test functions are taken from the space $\mathcal{Q}$.

The Dirichlet boundary conditions are imposed with the Nitsche's method as described in Chap. 2, with the parameter $\beta = 100$. Integration is conducted as described in Sec. 1.2. The skeleton stabilization technique is also utilized to eliminate potential oscillations. Both parameters in Eq. 2.5 are assigned the same value $\gamma = 0.05$. Typical velocity contours and pressure contours of the simulations are shown in Fig. 3.10.
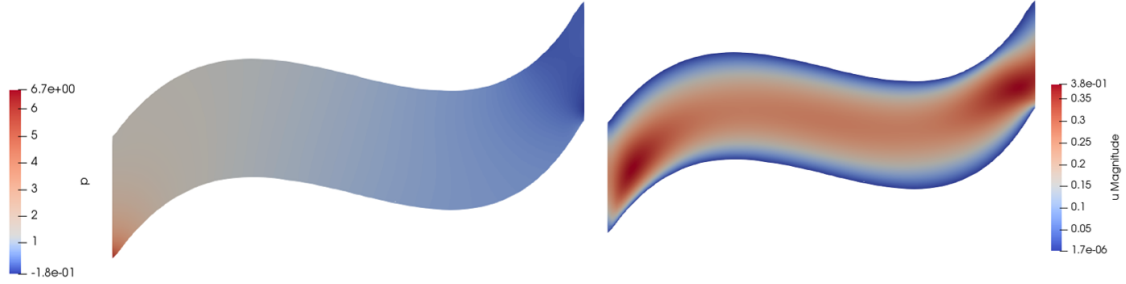

Figure 3.10: Velocity and pressure schemes resulting from simulation with the signed distance based immersogeometric analysis.

3.4 Extension to three dimensions

Three dimensional CAD models are much more complex than two dimensional models due to different operations to generate solid structures from sketches and surfaces, such as extrusion, sweeping, etc. The evaluation of the signed distance function for three dimensional CAD models with the method discussed in Section. 3.2.2 is not implemented in our research on account of its complexity. However, the location state of a random point with regard to a solid cad model can be inferred in an easier way, by counting the intersections between arbitrary ray lines passing through the query point and boundaries of the solid (see Fig. 3.11). Points from which all ray line have odd numbers of intersections with the boundary faces of the solid are located inside the solid. Points from which all ray lines have even numbers of intersections with the boundary face of the solid are located outside the solid. This algorithm is implemented in the open source package OPENCASCADE and is employed to extend our design through analysis method to three dimensional CAD models.
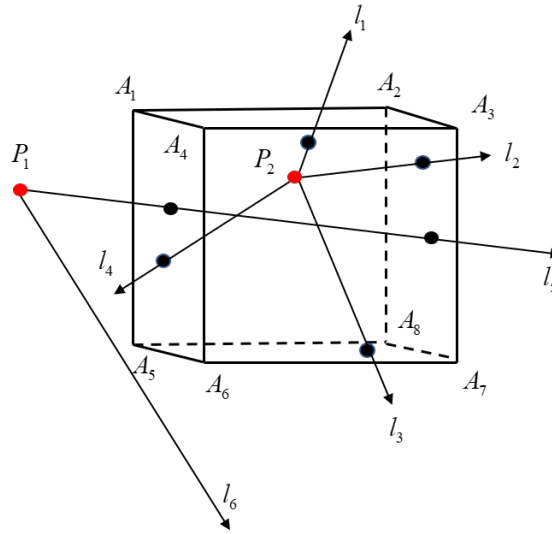
Figure 3.11: Location query by counting of intersections. Ray lines l_1, l_2, l_3, l_4 starting from the point P_2 inside the cube $A_1A_2A_3A_4A_5A_6A_7A_8$ each have only one intersection with the boundary faces of the solid. Ray lines l_5, l_6 starting from the point P_1 outside the cube have 2 or 0 intersections.

A simple 3D channel model is shown in Fig. 3.12. The levelset functions evaluated by location queries is shown in Fig. 3.13. Here the gray region is the trimmed area and the blue region is the levelset of the required domain. The curves are represented well by approximation with B-splines.

The same formulation as in Eq. 3.6 is studied on the domain shown in Fig. 3.12. Values of the density and the viscosity are set equal to properties of liquid water under normal temperature and pressure conditions. A parabolic velocity perpendicular to the inlet is imposed and the outlet is left free. The solid channel is considered without deformation, which is reasonable when the inflow flux is controlled at a low rate such that the Reynolds number is around 20, below the criterion $Re = 300$ as stated in Thompson et al. [36] to avoid turbulence and convection-dominated stability problems.
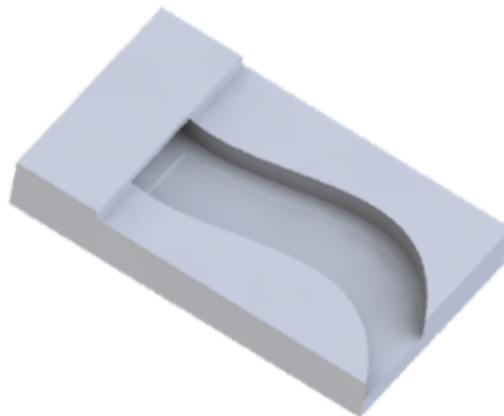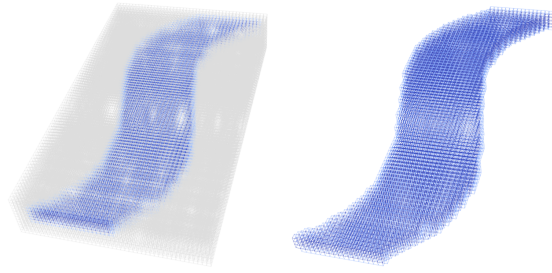

Figure 3.12: CAD model of a 3D planar simple model

Figure 3.13: Levelset functions evaluated with the location query method for the three dimensional simple model.

Chapter 4

Application to Tesla valves

Shape improvement of Tesla valves has been one of the topics of interests in fluid dynamics research (a review is given in the Section 1.1). There are many factors involved in the optimization of a Tesla valve, e.g., the inner angle, the aspect ratio of the cross section, the number of stages and the distance between stages. Therefore, this chapter presents a detailed numerical analysis of different designs of the Tesla valve. This analysis includes the geometry reconstruction from STEP/IGES data files and the periodic constraints with offsets (proposed in Chapter 3).

This chapter is outlined as follows. Section 4.1 illustrates the numerical analysis of different two-dimensional designs of the Tesla valve. Different three-dimensional designs are studied in Section 4.2.

4.1   Two dimensional shape improvements

The original geometry of the Tesla valve is referred to as T45-R because of its 45° inner angle (see Fig. 1.2). A classic alternative Tesla valve is the MT135 type (see Fig. 4.2a). Liao [18] compared the diodicity of a MT135 Tesla valve with a T45-R valve and concluded that the MT135 Tesla valve produces larger pressure differences for flows in opposite directions. As a validation, we will analyze this flow resisting behavior again with the help of the design-through-analysis workflow discussed in the previous chapter. The Navier-Stokes problem is studied herein to demonstrate the workflow (see Eq. 3.6). Properties of liquid water are used for the viscosity μ and the density ρ. The velocity at inlets is $1mm/s$ uniformly. The ambient domain is scaled to a unit square when element sizes are discussed.

A convergence study of the numerical method is conducted before studying different designs of the Tesla valve. The relation between relative errors of the flux and different element sizes h is studied for the MT135 Tesla valve. From this study, we observed that the relative error of the flux converges at a rate around 2 (depicted in the Fig. 4.1). When the element size $h < 0.02$, the solution is close to the reference solution and the relative error of the flux is smaller than 1%. Therefore, ambient meshes with the element size $h = 0.01$ are considered for the numerical study in the remainder of this chapter.

The T45-R and MT135 Tesla valves (see Fig. 4.2) are designed using the CAD software AUTOCAD and saved as STEP files. Thompson in [36] proved that flow in a Tesla valve is laminar when the Reynolds number is less than 300 at the inlet of the valve. For such low Reynolds numbers, it is reasonable to assume that the flow is steady. Therefore, the steady Navier-Stokes problem is considered for the analysis. A $5mm$ wide channel is considered. Given that the characteristic

length equals the width of the channel with square cross sections, the Reynolds number is around:

$$Re = \frac{\rho v L}{\mu} = 5 \tag{4.1}$$
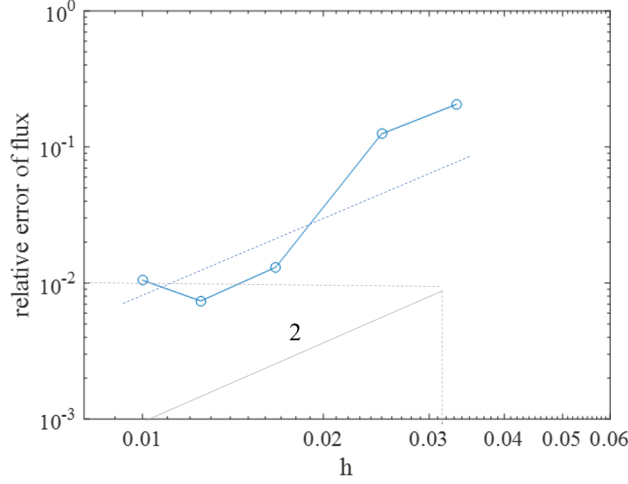

Figure 4.1: Relative errors of flux of the 2D MT135 Tesla valve for different mesh sizes h.

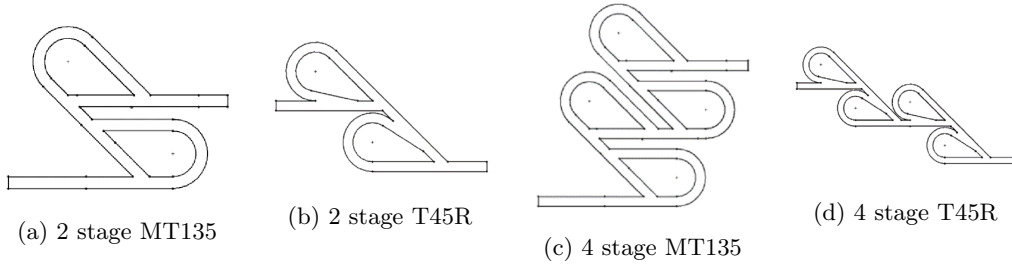(a) 2 stage MT135   (b) 2 stage T45R   (c) 4 stage MT135   (d) 4 stage T45R

Figure 4.2: T45R and MT135 Tesla valve with different stages

For different geometries, flows in the forward direction and the reverse direction are simulated. Pressures at the inlet and the outlet are recorded for the evaluation of the diodicity (which is the ratio of pressure differences for flows in opposite directions as shown in the Eq. 1.1). Diodicities of different valves are compared in Tab. 4.1.

Valve	2 stage MT135	2 stage TR45	4 stage MT135	4 stage TR45
diodicity	1.026	1.000	1.011	1.005

Table 4.1: Diodicity of the different T45-R and MT135 Tesla valve for the Reynolds number $Re = 5$

The comparison of the diodicity qualitatively validates the flow resisting property of the Tesla valve since diodicities of all valves are always above 1. The diodicity of MT135 Tesla valves is larger than that of T45-R Tesla valves. This shows that the MT135 Tesla valve has better flow resisting ability and it can be preferred in cases where highly flow resisting properties are required. The diodicity of the 4 stage MT135 Tesla valve is smaller than that of the 2 stage MT135 Tesla

valve. In order to understand it better, the influence of the number of stages on diodicity is studied in detail.

number of stages	2	4	6	8
diodicity	1.026	1.012	1.036	1.074

Table 4.2: Diodicity of the 2D MT135 Tesla valve for the different number of stages for the Reynolds number $Re = 5$

The diodicity of MT135 Tesla valves with different stages is studied and compared in Tab. 4.3 and Fig. 4.3. From Tab. 4.3 and Fig. 4.3, we observed that increasing the number of stages in Tesla valves will in general promote the flow resisting ability of the valve. However, the influence of the number of stages on the diodicity is relatively small (see Tab. 4.1). Therefore, increasing the number of stages is not a natural choice when a large enhancement is required for the flow resisting ability of the Tesla valve.
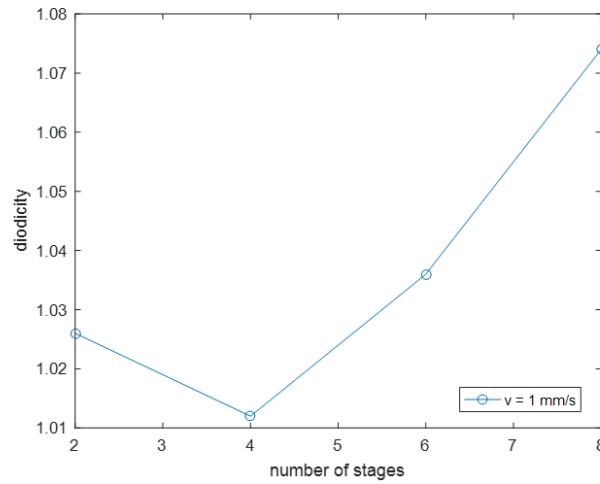
Figure 4.3: The diodicity of the 2D MT135 Tesla valve for different numbers of stages

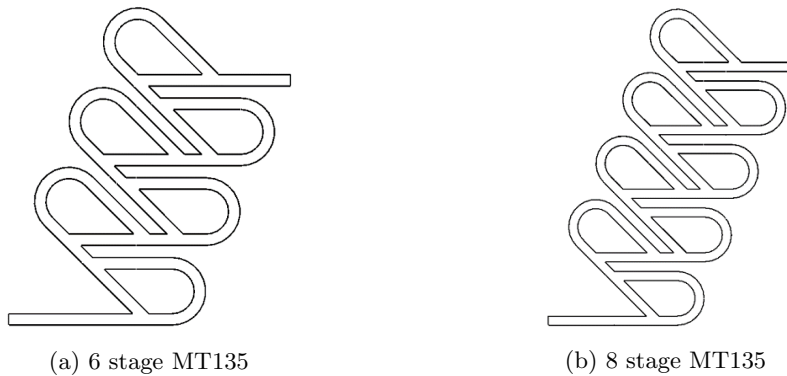
(a) 6 stage MT135   (b) 8 stage MT135

Figure 4.4: MT135 Tesla valve with different number of stages

Furthermore, MT135 Tesla valves with 6 and 8 stages (shown in Fig. 4.4) are considered for the numerical analysis of the steady Navier-Stokes flow. The velocity and the pressure profiles are presented in the Fig. 4.7. From this analysis we observed the following The pressure drops

progressively in the channel. For $Re = 5$, the flow concentrates in the main part of the channel and seldom goes through arcs of the channel. Differences between flows in the forward direction and in the reverse direction are hardly visible on account of the low Reynolds number.
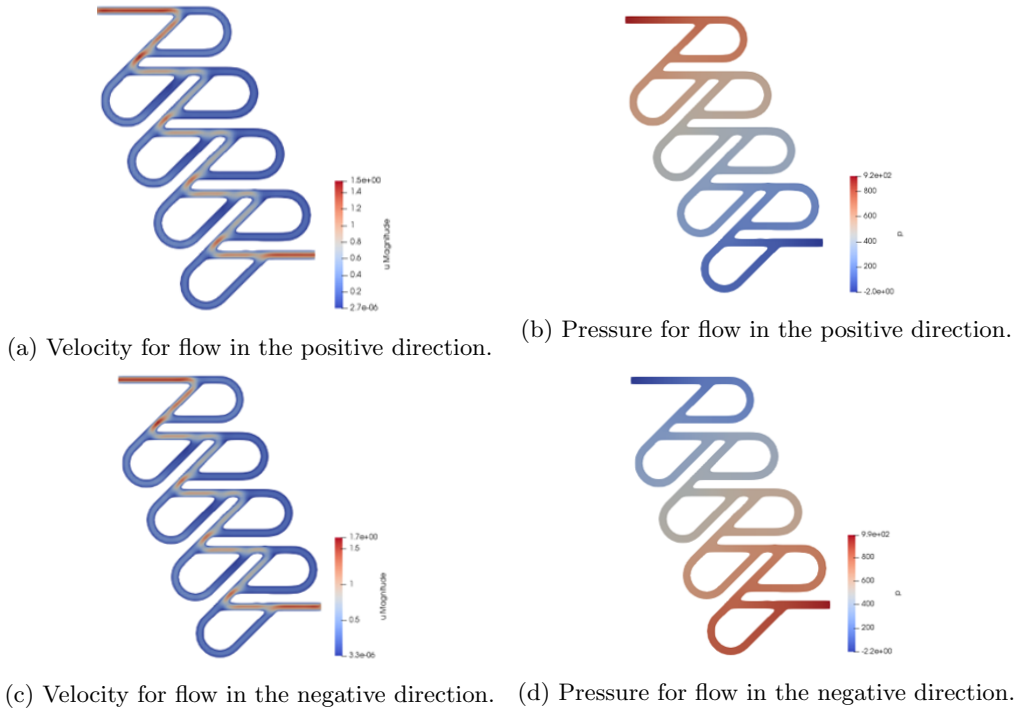

(a) Velocity for flow in the positive direction.

(b) Pressure for flow in the positive direction.

(c) Velocity for flow in the negative direction.

(d) Pressure for flow in the negative direction.

Figure 4.5: Velocity and pressure profiles of the flow in the MT135 Tesla valve with 8 stages for the Reynolds number $Re = 5$
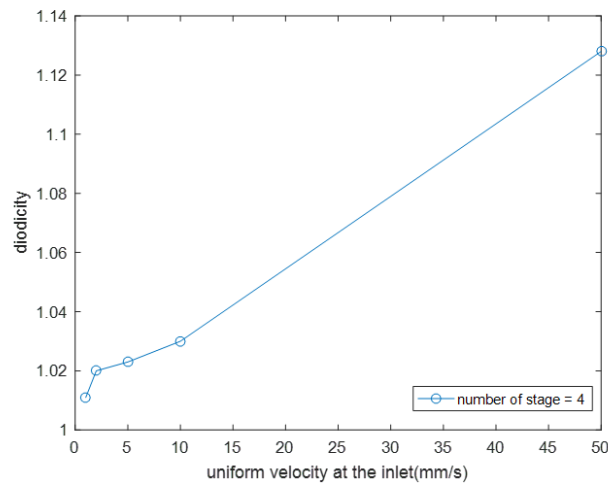
Figure 4.6: The diodicity of the MT135 Tesla valve (with four stages) for different inlet velocities

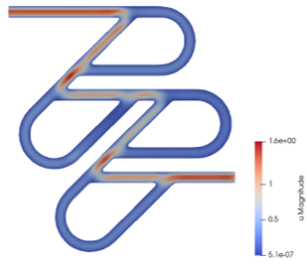| velocity(mm/s)	1	2	5	10	50
Reynolds number	5	10	25	50	250
diodicity	1.012	1.020	1.023	1.030	1.128

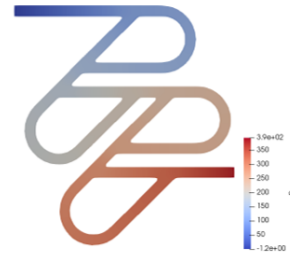Table 4.3: Diodicity for the MT135 type Tesla valves with different Reynolds numbers.
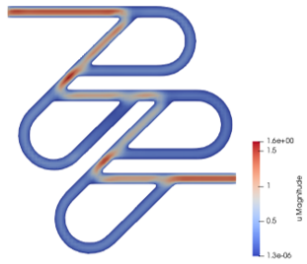
(a) The velocity for the flow in the positive direction. $Re = 1$
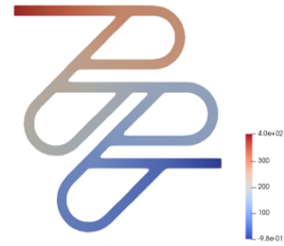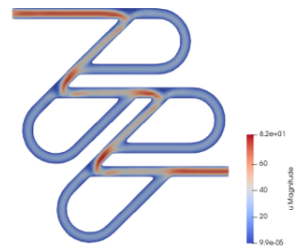

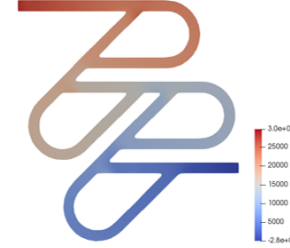(b) The pressure for flow in the positive direction. $Re = 1$

(c) Velocity for forward flow. $Re = 1$
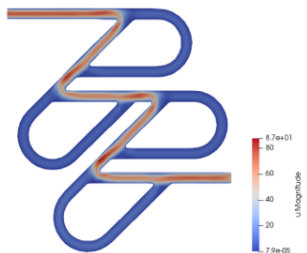

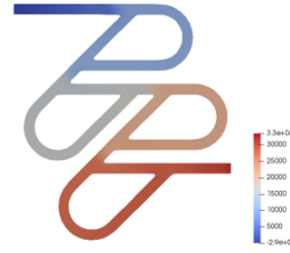(d) Pressure for reverse flow. $Re = 1$

(e) Velocity for forward flow. $Re = 50$

(f) Pressure for reverse flow. $Re = 50$

(g) Velocity for forward flow. $Re = 50$

(h) Pressure for reverse flow. $Re = 50$

Figure 4.7: The velocity and pressure fields of the MT135 Tesla valve (with four stages) for the Reynolds numbers $Re = 1$ and $Re = 50$.

In the literature it has been reported that the inlet velocity of the flow has a significant influence on the flow resistance of Tesla valves. Therefore, flow resisting behaviors for different inlet velocities are also studied for a two stage MT135 Tesla valve (see Fig. 4.6). We observed the following:

The diodicity is approximately proportional to the inlet velocity. Changes of pressures are always progressive. For the Reynolds number $Re = 1$, profiles are similar for flows in opposite directions. However, for the Reynolds number $Re = 50$, the velocity profile of the forward direction flow is very distinguished from the reverse direction flow by recognizable flow in the arcs of the Tesla valve. Therefore, a prerequisite to utilize the flow resistance of Tesla valves is to have flows with relatively high Reynolds numbers.

4.2 Three dimensional shape improvements

A three dimensional Tesla valve is built in Solidworks (CAD software) as shown in Fig. 4.8 and is saved as a STEP data file.
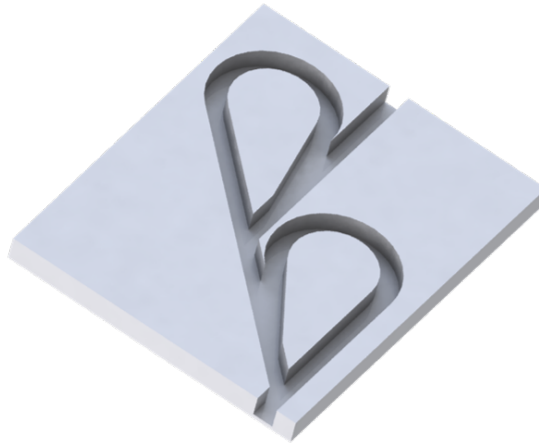

Figure 4.8: Solidworks CAD model of the three dimensional Tesla valve which is saved as a STEP data file.

With the help of the STEP file, the levelset functions (see Fig. 4.9) are evaluated with the location query method and are smoothed with the convolution method as described in Chapter 3. The degree of splines used in the convolution to approximate the levelset functions has a significant influence on the accuracy of the representation (see Fig. 4.10). Therefore, the degree of splines can be increased to obtain accurate geometry reconstruction from the CAD data file. Due to unaffordable computational costs, the second order splines (which results in a fairly good reconstruction of the geometry from the CAD data file) are considered in this work. However, the geometry reconstructed with the second order splines fails to approximate perpendicular planar faces and sharp corners. A potential solution is to refine the mesh. But this is not implemented in our research due to limitations of computational resources.

The Stokes problem (Eq. (2.8)) is investigated in the 3D Tesla valve. The uniform inlet velocity is taken as $10mm/s$. The dynamic viscosity μ is taken from the properties of water. The characteristic length of the flow is taken as the width of the square channel $L = 10 \quad mm$. The Reynolds number is evaluated as $Re = \frac{Lv}{\mu} = 100$. The length of the ambient domain is scaled to the unit length in the x direction when element sizes are discussed. The pressure profile is shown in Fig 4.12. Different planes are considered to illustrate the velocity profiles and are presented in Figs. 4.11 and 4.13.
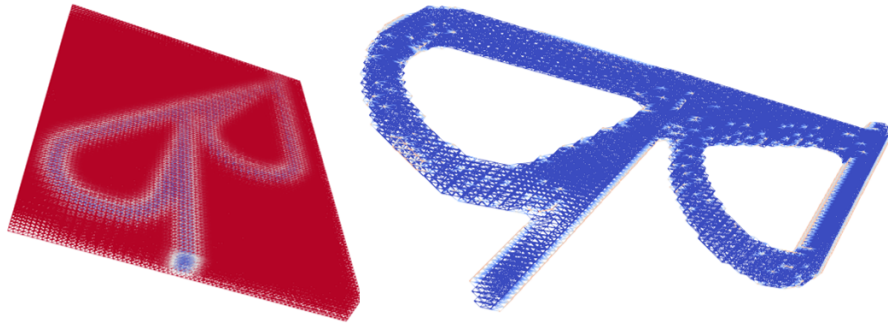
Figure 4.9: (left) Levelset functions of the three dimensional Tesla valve. (right) Point representation of the three dimensional segmented flow channel.
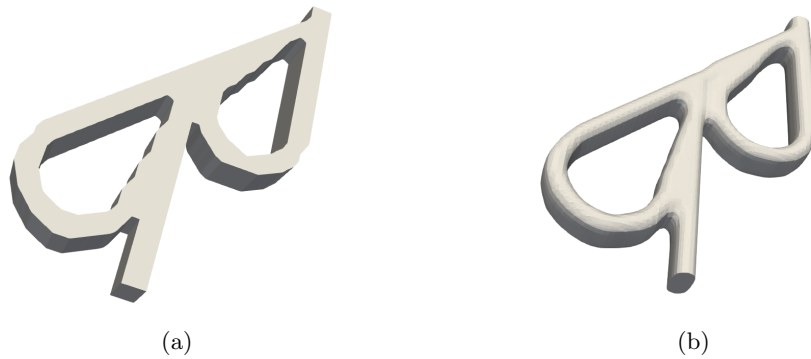

(a)   (b)

Figure 4.10: Reconstructed geometries approximated by splines of different degrees k: (a) $k = 1$, (b) $k = 2$.
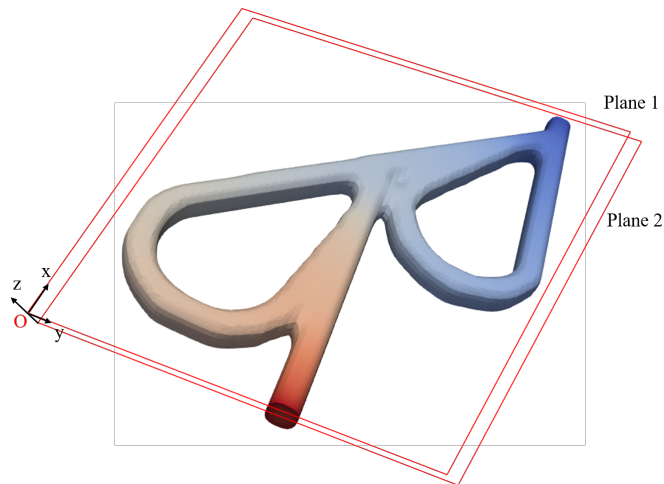

Figure 4.11: Definition of two planes parallel to the x-y plane (Plane 1 is above Plane 2).

In this study we observed the following: the pressure difference is very similar at different heights of the channel. However, velocity profiles show that the flux tends to concentrate at the center of the channel (see Fig. 4.13 and Fig. 4.13). Flow prefers the main channels (i.e., Channel 2 and 3) compared to the side channels (i.e., Channel 1 and 4). This flow pattern is in agreement with the

working principle of Tesla valves which qualitatively validates our numerical method.

(a) Velocity in Plane 1.

(b) Pressure in Plane 1.

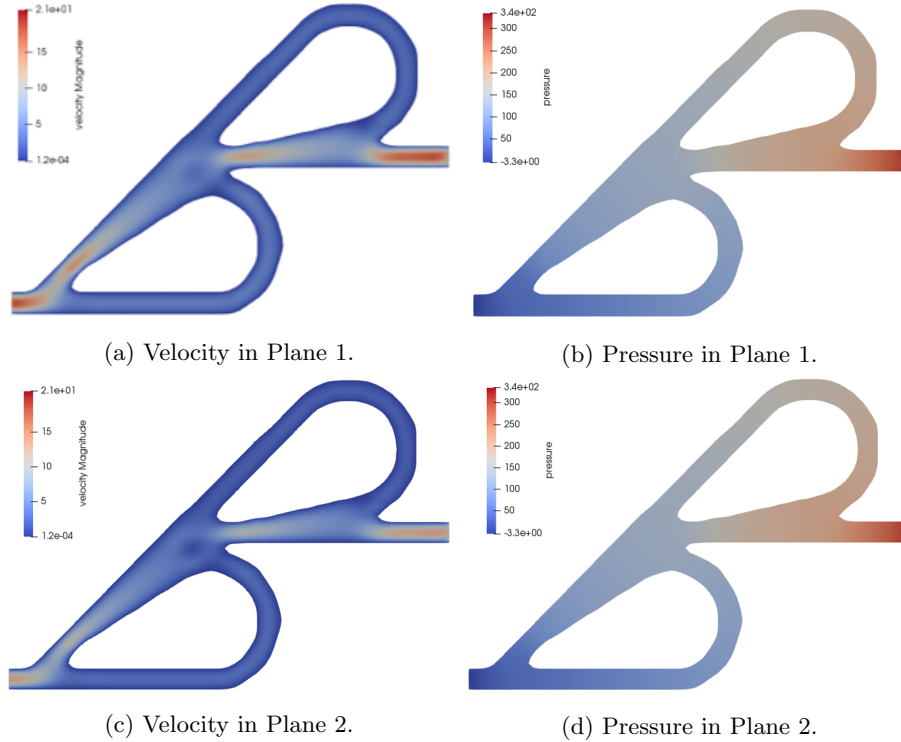(c) Velocity in Plane 2.

(d) Pressure in Plane 2.

Figure 4.12: The velocity and pressure profiles of the Stokes flow in the three dimensional Tesla valve in two planes parallel to the x-y plane.

The relative error of the flux is studied with different mesh sizes (see Fig. 4.14). It converges with an optimal rate of 4. Considering the magnitude of the relative errors, an element size of $h=0.02$ is considered for further simulations.
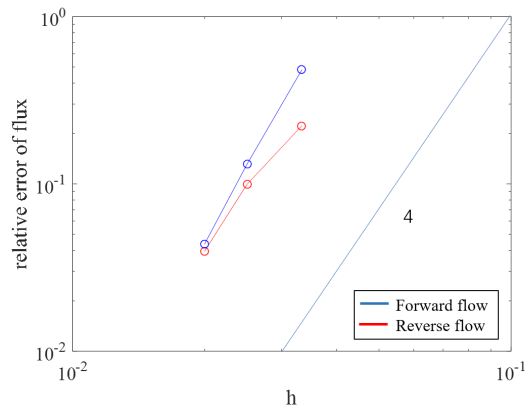

Figure 4.14: The relative error of the flux for different mesh sizes h.

So far the Tesla valve with the square cross section 10 $mm \times 10$ mm is considered for the analysis. The flow is also significantly influenced by the aspect ratio of the cross-section area of valves which therefore is an important aspect to study. Tesla valves with rectangular cross section

shape($mm \times mm$)	15.0×7.5	10.0×10.0	8.3×12.5	7.5×15.0
aspect ratio	0.5	1	1.5	2
diodicity	1.325	1.334	1.329	1.284

Table 4.4: The diodicity of a 3D Tesla valve with different cross sections

of different aspect ratios ($15.0mm \times 7.5mm$, $10.0mm \times 10.0mm$, $8.3mm \times 12.5mm$, $7.5mm \times 15.0mm$, see Fig. 4.15) are considered and the Stokes flow is studied. The length a and the width b of the cross section are chosen to maintain the characteristic length of the channel in accordance with the definition:

$$L = \frac{2ab}{a + b} \tag{4.2}$$

The considered parameters are: the uniform inlet velocity $v = 10mm/s$, the Reynolds number $Re = 100$. Pressures at both ends of the channel for opposite flow directions are recorded. The diodicity is evaluated and compared (see Tab. 4.4). It is observed that the square shaped Tesla valve is the optimal shape of the cross section. This conclusion is consistent with the results reported by Zhang et al. [43].


(a)

(b)

(c)

(d)
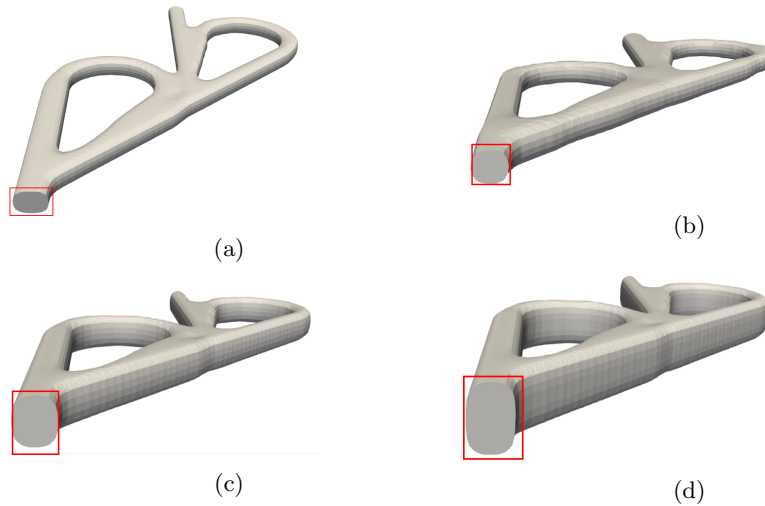
Figure 4.15: Rectangular cross sections with different aspect ratios: (a) $15.0mm \times 7.5mm$ (b) $10.0mm \times 10.0mm$ (c) $8.3mm \times 12.5mm$ (d) $7.5mm \times 15.0mm$.

In this chapter, the influence of several design parameters on the flow resisting behavior of Tesla valves has been studied. Through this study, we demonstrated the capability of the proposed workflow. Here, change of each parameter leads to a new CAD model and little time-consuming manual work by the user is required to conduct the numerical analysis. This contrast the traditional FEM workflow, which takes quite a lot of work to perform various simulations. The workflow proposed herein reduces the work load of the simulation of a new CAD model by saving it as a new STEP data file, while not requiring further changes to the simulation setup.
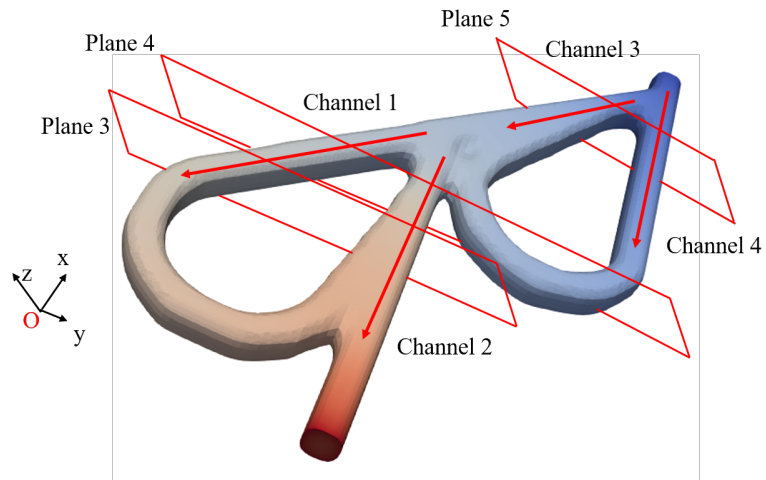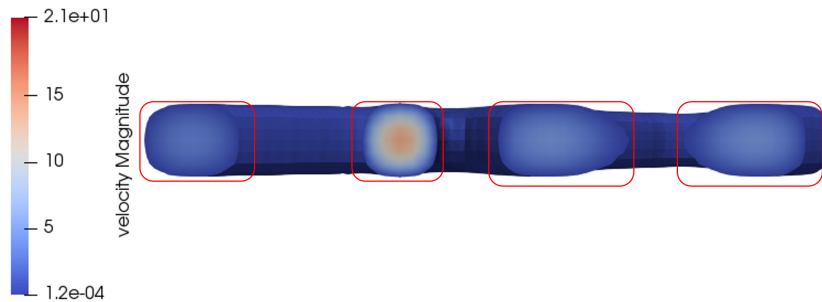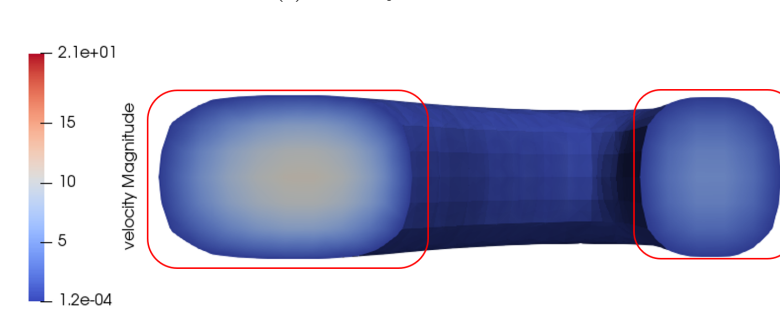
(a) Position of clipping planes.
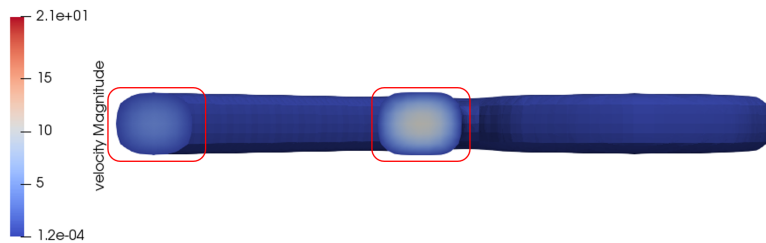
(b) Velocity in Plane 3.

(c) Velocity in Plane 4.

(d) Velocity in Plane 5.

Figure 4.13: Results of the simulation for the Stokes problem in the three dimensional Tesla valve in planes parallel to the y-z plane.

Chapter 5

Conclusion

Numerical analysis techniques in additive manufacturing can be used to increase productivity. Conventional workflows involve frequent communication between design and numerical analysis departments. Any small change of design parameters calls for a completely new simulation. This is not only expensive but also time consuming. A design-through-analysis workflow is proposed in this thesis to reduce the repetitive communication and unnecessary user efforts. This analysis workflow is based on the concept of immersogeometric analysis. 3D printed fluid devices are considered as the application of choice.

One of the main contributions of this work is the CAD-based geometry reconstruction. We have developed functions in Nutils (Python-based numerical utilities library) to read CAD data files (STEP/IGES files) and to extract required information for the geometry reconstruction. The levelset based framework to reconstruct geometry proposed in Ref. [39] is adjusted and employed. Algorithms to evaluate signed distance functions for boundary represented models are presented. The framework is extended to three dimensional cases by generating levelset functions using the developed location query method. Implementations of these approaches are presented with details.

Additionally, we have introduced a formulation where periodic boundary conditions are imposed by Nitsche's method in the immersogeometric analysis setting. Functions are developed in Nutils to implement these constraints. The assumption of flow periodicity in Tesla valves is reasonable since only flows with small Reynolds numbers are considered in the thesis. For convection-dominated flows with high Reynolds numbers, further developments to the method are required for stabilization. The strategy to shift the ambient domain proposed in this thesis avoids complex point projection methods used in conventional methods.

With the immersogeometric analysis and approaches to reconstruct the geometry, a straightforward and relatively comprehensive workflow can be employed in prototypical cases. Applications of the workflow in shape improvements of Tesla valves are discussed. The convenience and the potential of the workflow are presented with a few examples. Modifications of parameters in the design process are contained within CAD data files and are instantly adopted in simulations without the need for time-consuming geometry clean-up and meshing operations.

For further development, we aim to better control the accuracy of the framework and to explore more applications of the workflow. The proposed method can be extended to convection-dominated problems, but additional stabilization techniques are required in such situations. In this thesis, low order refinements and relatively coarse ambient meshes are employed due to limitations of computational resources. With high order discretizations and fine ambient meshes, better accuracy can be expected and more applications can be taken into consideration. Enhancements in the computing efficiency by code optimization is also a target of future work.

Bibliography

[1] BlanchardAfromowitz-M. A. A. P. Forster F. K. Afromowitz, M. A. and N. R. Sharma. Micropumps with fixed valves, 1999. U.S. Patent NO. 5876187.

[2] Chrif Amrouche, Macaire Batchi, and Jean Batina. Navierstokes equations with periodic boundary conditions and pressure loss. *Applied Mathematics Letters*, 20(1):48 – 53, 2007.

[3] S.F. de Vries, D. Florea, F.G.A. Homburg, and A.J.H. Frijns. Design and operation of a tesla-type valve for pulsating heat pipes. *International Journal of Heat and Mass Transfer*, 105:1 – 11, 2017.

[4] Maik Dittmann. *Isogeometric analysis and hierarchical refinement for multi-field contact problems*, volume 4. KIT Scientific Publishing, 2017.

[5] Xiaoxiao Du, Gang Zhao, and Wei Wang. Nitsche method for isogeometric analysis of reiss-nermindlin plate with non-conforming multi-patches. *Computer Aided Geometric Design*, 35-36:121 – 136, 2015.

[6] Fred K Forster, Ronald L Bardell, Martin A Afromowitz, Nigel R Sharma, and Alan Blanchard. Design, fabrication and testing of fixed-valve micro-pumps. *ASME-PUBLICATIONS-FED*, 234:39–44, 1995.

[7] Morris-C. J. Gamboa, A. R. and F. K. Forster. Improvements in fixed-valve micropump performance through shape optimization of valves. *ASME J. Fluid Eng.*, 127:339–346, 2005.

[8] Yujie Guo, Jason Heller, Thomas J.R. Hughes, Martin Ruess, and Dominik Schillinger. Variationally consistent isogeometric analysis of trimmed thin shells at finite deformations, based on the step exchange format. *Computer Methods in Applied Mechanics and Engineering*, 336:39 – 79, 2018.

[9] Yujie Guo and Martin Ruess. Nitsches method for a coupling of isogeometric thin shells and blended shell structures. *Computer Methods in Applied Mechanics and Engineering*, 284:881 – 905, 2015.

[10] Tuong Hoang, Clemens V Verhoosel, Ferdinando Auricchio, E Harald van Brummelen, and Alessandro Reali. Mixed isogeometric finite cell methods for the stokes problem. *Computer Methods in Applied Mechanics and Engineering*, 316:400–423, 2017.

[11] Tuong Hoang, Clemens V Verhoosel, Ferdinando Auricchio, E Harald van Brummelen, and Alessandro Reali. Skeleton-stabilized isogeometric analysis: High-regularity interior-penalty methods for incompressible viscous flow problems. *Computer Methods in Applied Mechanics and Engineering*, 337:324–351, 2018.

[12] Tuong Hoang, Clemens V. Verhoosel, Chao-Zhong Qin, Ferdinando Auricchio, Alessandro Reali, and E. Harald van Brummelen. Skeleton-stabilized immersogeometric analysis for incompressible viscous flow problems, 2018.

[13] Ming-Chen Hsu, Chenglong Wang, Fei Xu, Austin J. Herrema, and Adarsh Krishnamurthy. Direct immersogeometric fluid flow analysis using b-rep cad models. *Computer Aided Geometric Design*, 43:143 – 158, 2016.

[14] Thomas JR Hughes, John A Cottrell, and Yuri Bazilevs. Isogeometric analysis: Cad, finite elements, nurbs, exact geometry and mesh refinement. *Computer methods in applied mechanics and engineering*, 194(39-41):4135–4195, 2005.

[15] Mika Juntunen and Rolf Stenberg. Nitsches method for general boundary conditions. *Mathematics of computation*, 78(267):1353–1374, 2009.

[16] Hsu M.-C. Schillinger D. Evans J. A. Aggarwal A. Bazilevs Y. Hughes T. J. R. Kamensky, D. An immersogeometric variational framework for fluidstructure interaction: application to bioprosthetic heart valves. *Computer Methods in Applied Mechanics and Engineering*, 284:10051053, 2015.

[17] Fredrik Larsson, Kenneth Runesson, Sepehr Saroukhani, and Reza Vafadari. Computational homogenization based on a weak format of micro-periodicity for rve-problems. *Computer Methods in Applied Mechanics and Engineering*, 200(1-4):11–26, 2011.

[18] P. F. Liao. A study on no-moving-part valves for flows in microchannels. Master's thesis, Department of Aeronautics and Astronautics, National Cheng Kung University, China.

[19] YingLiang Ma and W. Terry Hewitt. Point inversion and projection for nurbs curve and surface: Control polygon approach. *Computer Aided Geometric Design*, 20:79–99, 2003.

[20] Benjamin Marussig and Thomas JR Hughes. A review of trimming in isogeometric analysis: Challenges, data exchange and simulation aspects. *Archives of computational methods in engineering*, pages 1–69, 2017.

[21] Kjell Magne Mathisen, Knut Morten Okstad, Trond Kvamsdal, and Siv Bente Raknes. Isogeometric analysis of finite deformation nearly incompressible solids. *Journal of Structural Mechanics*, 44(3):260–278, 2011.

[22] Rajat Mittal and Gianluca Iaccarino. Immersed boundary methods. *Annu. Rev. Fluid Mech.*, 37:239–261, 2005.

[23] Kolahdouz M. E. Shirani E. Mohammadzadeh, K. and M. B. Shafii. Numerical investigation on the effect of the size and number of stages on the tesla microvalve efficiency. *J. Mech.*, 29:527–534, 2012.

[24] Jamshid Parvizian, Alexander Düster, and Ernst Rank. Finite cell method. *Computational Mechanics*, 41(1):121–133, 2007.

[25] C. S. Peskin. The immersed boundary method. *Acta Numerica.*, 11:479–517, 2002.

[26] Les Piegl and Wayne Tiller. *The NURBS book*. Springer Science & Business Media, 2012.

[27] Ernst Rank, Martin Ruess, Stefan Kollmannsberger, Dominik Schillinger, and Alexander Düster. Geometric modeling, isogeometric analysis and the finite cell method. *Computer Methods in Applied Mechanics and Engineering*, 249:104–115, 2012.

[28] J. L. Reed. Fluidic rectifier, 1993. U.S. Patent NO. 5265636.

[29] FJP Reis and FM Andrade Pires. A mortar based approach for the enforcement of periodic boundary conditions on arbitrarily generated meshes. *Computer Methods in Applied Mechanics and Engineering*, 274:168–191, 2014.

[30] Jessica D. Sanders, Tod A. Laursen, and Michael A. Puso. A nitsche embedded mesh method. *Computational Mechanics*, 49:243–257, 2012.

[31] Dominik Schillinger, Luca Dede, Michael A Scott, John A Evans, Michael J Borden, Ernst Rank, and Thomas JR Hughes. An isogeometric design-through-analysis methodology based on adaptive hierarchical refinement of nurbs, immersed boundary methods, and t-spline cad surfaces. *Computer Methods in Applied Mechanics and Engineering*, 249:116–150, 2012.

[32] Dominik Schillinger and Ernst Rank. An unfitted hp-adaptive finite element method based on hierarchical b-splines for interface problems of complex geometry. *Computer Methods in Applied Mechanics and Engineering*, 200(47-48):3358–3380, 2011.

[33] Dominik Schillinger and Martin Ruess. The finite cell method: A review in the context of higher-order structural analysis of cad and image-based geometric models. *Archives of Computational Methods in Engineering*, 22(3):391–455, 2015.

[34] Erik Svenning, Martin Fagerström, and Fredrik Larsson. Computational homogenization of microfractured continua using weakly periodic boundary conditions. *Computer Methods in Applied Mechanics and Engineering*, 299:1–21, 2016.

[35] N. Tesla. Valvular conduit, 1920. U.S. Patent NO. 1329559.

[36] Paudel B.J. Jamal T. Thompson, S.M. and D.K. Walters. Numerical investigation of multi-staged tesla valves. *Journal of Fluids Engineering*, 136:081102, 2014.

[37] T. Q. Truong and N. T. Nguyen. Simulation and optimization of tesla valves. In *Nanotech - Nanotechnology Conference and Trade Show*, pages 178–181, 2003.

[38] Vasco Varduhn, Ming-Chen Hsu, Martin Ruess, and Dominik Schillinger. The tetrahedral finite cell method: Higher-order immersogeometric analysis on adaptive non-boundary-fitted meshes. *International Journal for Numerical Methods in Engineering*, 107:1054–1079, 2016.

[39] Clemens V Verhoosel, GJ Van Zwieten, B Van Rietbergen, and René de Borst. Image-based goal-oriented adaptive isogeometric analysis with application to the micro-mechanical modeling of trabecular bone. *Computer Methods in Applied Mechanics and Engineering*, 284:138–164, 2015.

[40] Rongqiao Wang, Long Zhang, Dianyin Hu, Chunhui Liu, Xiuli Shen, Chongdu Cho, and Bo Li. A novel approach to impose periodic boundary condition on braided composite rve model based on rpim. *Composite Structures*, 163:77–88, 2017.

[41] Fei Xu, Dominik Schillinger, David Kamensky, Vasco Varduhn, Chenglong Wang, and Ming-Chen Hsu. The tetrahedral finite cell method for fluids: Immersogeometric analysis of turbulent flow around complex geometries. *Computers and Fluids*, 141:135 – 154, 2016.

[42] Zheng Yuan and Jacob Fish. Toward realization of computational homogenization in practice. *International Journal for Numerical Methods in Engineering*, 73(3):361–380, 2008.

[43] S Zhang, SH Winoto, and HT Low. Performance simulations of tesla microfluidic valves. In *2007 First International Conference on Integration and Commercialization of Micro and Nanosystems*, pages 15–19. American Society of Mechanical Engineers, 2007.

TU/e
Technische Universiteit
Eindhoven
University of Technology

Declaration concerning the TU/e Code of Scientific Conduct
for the Master's thesis

I have read the TU/e Code of Scientific Conduct[i].

I hereby declare that my Master's thesis has been carried out in accordance with the rules of the TU/e Code of Scientific Conduct

Date

.......29 Aug 2018...................

Name

.......Fankai Peng..........................

ID-number

.......1038461...........................

Signature

.......Fankai Peng.......................

Submit the signed declaration to the student administration of your department.

January 15 2016